
A UNIFIED SPATIOTEMPORAL FRAMEWORK FOR MODELING CENSORED AND MISSING AREAL RESPONSES

Jose A. Ordoñez

Department of Statistics
Pontificia Universidad Católica de Chile
Santiago, PA 782 0436
jose.ordonez@uc.cl

Tsung-I Lin

Institute of Statistics, National Chung Hsing University
Department of Public Health, China Medical University
tilin@nchu.edu.tw

Victor H. Lachos

Department of Statistics
University of Connecticut
hlachos@uconn.edu

Luis M. Castro

Department of Statistics
Pontificia Universidad Católica de Chile
Santiago, PA 782 0436
lmcastro@uc.cl

November 26, 2025

ABSTRACT

We propose a new Bayesian approach for spatiotemporal areal data with censored and missing observations. The method introduces a flexible random effect that combines the spatial dependence structures of the Simultaneous Autoregressive (SAR) and Directed Acyclic Graph Autoregressive (DAGAR) models with a temporal autoregressive component. We demonstrate that this formulation extends both spatial models into a unified spatiotemporal framework, expressing them as Gaussian Markov random fields in their innovation form. The resulting model captures spatial, temporal, and joint spatiotemporal correlations in an interpretable way. Simulation studies show that the proposed model outperforms common ad hoc imputation strategies, such as replacing censored values with the limit of detection (LOD) or imputing missing data by the sample mean. We further apply the method to carbon monoxide (CO) concentration data from Beijing's air quality network, comparing the proposed DAGAR-AR model with the traditional Conditional Autoregressive (CAR) approach. The results indicate that while the CAR model achieves slightly better predictive performance, the DAGAR-AR specification offers clearer interpretability and a more coherent representation of the spatiotemporal dependence structure.

1 Introduction

According to the U.S. Environmental Protection Agency (EPA), carbon monoxide (CO) is a colorless, odorless, tasteless, poisonous, and flammable gas produced by the incomplete oxidation of carbon during combustion. Common community sources of CO include chimneys, gas stoves, space heaters, water heaters and wood stoves. Low-level exposure to CO may cause fatigue and chest pain in individuals with pre-existing heart disease, whereas higher levels of exposure can lead to headaches, dizziness and confusion. At sufficiently elevated concentrations, CO exposure can be fatal [13].

From a public health perspective, CO pollution is of particular concern because short-term exposure is significantly associated with daily mortality [7]. Furthermore, as noted by Raub [15], in some regions, CO levels are strongly correlated with particulate matter, such as PM10¹, especially during winter months. These particles are detrimental to health, contributing to an increased risk of cardiovascular mortality and hospitalization [1].

¹PM10 and PM2.5 denote particulate matter suspended in the air with a diameter of 10 micrometers or less, and 2.5 micrometers or less, respectively, which is sufficiently small to be inhaled and reach deep into the pulmonary system.

In the statistical literature, several proposals have addressed the modeling of CO or pollution components within a spatio-temporal framework. For instance, de Luna and Genton [9] introduced a novel family of predictive spatio-temporal models tailored explicitly for environmental data, focusing on CO concentrations in Venice, which are characterized by spatial sparsity and temporal richness. The core methodology employs a vector autoregressive (VAR) specification, treating each monitoring station as a time series, and a distinctive model-building strategy that facilitates the identification of spatial dependencies.

Wang and Sun [20] presented a penalized local polynomial regression model developed for spatial data analysis, intending to address spatial heterogeneity in regression coefficients. The authors proposed a methodology for examining environmental variables, such as PM_{2.5} concentrations and various pollutant gases in China, by representing spatially varying parameters as a combination of local polynomials at designated “anchor points”. This approach employs a penalized least-squares procedure to estimate these parameters, promoting local homogeneity.

In contrast, Deb and Tsay [10] introduced a spatiotemporal model tailored to analyze air pollution data, focusing on PM_{2.5} concentrations and identifying space–time interactions. In this framework, an interaction implies that temporal pollution trends are more similar among sites in close spatial proximity. The study applied this model to a ten-year dataset collected from 66 monitoring stations across Taiwan, addressing a gap in the literature on air pollution in Asian contexts.

Recently, Valeriano et al. [18] extended the spatiotemporal modeling framework by introducing separable correlation structures and implementing the Stochastic Approximation Expectation–Maximization (SAEM) algorithm for parameter inference. The SAEM procedure facilitates the maximum likelihood estimation in complex settings by iteratively approximating the expectation step through stochastic simulations. Missing and censored data are accommodated by augmenting the complete data formulation and modeling the unobserved values using truncated normal distributions. Although their empirical application did not involve CO or particulate matter, the methodology was illustrated using ozone concentration data from New York.

A key component in assessing the health impacts of CO pollution within a given city is the statistical modeling of ambient CO concentrations. However, this process entails several methodological challenges. These include accounting for the temporal and spatial variability in pollutant levels, addressing potential censored and missing data, and selecting appropriate covariates to capture meteorological and seasonal effects. Including these particulars in the analysis is necessary to obtain valid and coherent conclusions.

Our proposal intends to provide a novel spatiotemporal model that considers censoring and missingness mechanisms, treating them as informative features rather than nuisance features. Moreover, because the data we analyzed are areal data, we considered the use of direct acyclic graph autoregressive (DAGAR) models [see 8]. This model provides a novel framework for the study of areal spatial models using a direct acyclic graph (DAG). The advantage of using a DAG is that it allows us to represent the spatial correlation structure of zones in a particular city in a simple and sparse manner. More precisely, a DAG provides a natural scheme to determine the neighbors of each zone, allowing us to establish the dependency structures of the observations over the location of interest. It is important to stress that one of the essential features of DAGAR models is that they are more robust than other competitive models, such as the conditional autoregressive [CAR; 6] and simultaneous autoregressive [SAR; 22] models. The DAGAR approach builds spatial correlation matrices generating positive definite and sparse matrices compared to popular tools such as CAR and SAR models.

The remainder of this paper is organized as follows. Section 3 introduces the model and defines a new spatiotemporal effect based on the DAGAR model. Section 4 presents the Bayesian inference under specified priors, where the missing and censored values are treated as latent random variables. Section 5 reports a simulation study that evaluates the estimation and prediction performance. Section 6 illustrates the methodology using a real dataset. Finally, some concluding remarks are presented in 7.

2 The Beijing multi-station air quality dataset

The dataset analyzed in this study originated from the Beijing air pollution monitoring network, which was established in January 2013 as part of a nationwide environmental surveillance program. Between 2013 and 2017, hourly observations of multiple air pollutants, including carbon monoxide (CO), and key meteorological variables, such as temperature and wind speed, were collected from 12 monitoring stations distributed across Beijing. Notably, this dataset provides a comprehensive spatiotemporal record of urban air quality dynamics. The dataset is publicly accessible through the UCI Machine Learning Repository (<https://archive.ics.uci.edu>).

One of the earliest studies to analyze this dataset was conducted by Zhang et al. [23], who investigated the temporal behavior of PM_{2.5} concentrations in Beijing. Their results indicated that air pollution levels in 2016 had likely been

underestimated, as previous reports suggested a 9.9% decline in the annual PM2.5 concentrations. More recently, Wardana et al. [21] employed the same dataset to develop an autoencoder-based model incorporating spatiotemporal components to estimate missing air pollutant observations.

In this study, we modeled CO concentrations ($\mu\text{g}/\text{m}^3$) collected twice daily at 09:00 and 19:00, which correspond to peak traffic periods. The analysis covered the period from November 25, 2016, to February 28, 2017, and included observations from 12 monitoring sites, each recorded at 190 time points, resulting in a total of 2280 observations (12×190). There were 55 missing values. The final three days (26/02/2017–28/02/2017) were reserved as a test dataset for all stations to assess the predictive performance of the proposed model. Accordingly, model training was conducted using $12 \times 184 = 2208$ observations, whereas testing involved $12 \times 6 = 72$ observations. This study period coincided with the winter season in Beijing, during which CO concentrations are typically elevated owing to increased heating demand and stable atmospheric conditions that restrict pollutant dispersion.

To mitigate the influence of extreme values and reduce issues related to variance heterogeneity, analysis was conducted using CO concentrations expressed on a logarithmic scale. A raw scatter plot of the log-transformed CO concentrations along the monitoring stations is shown in Figure 1. It can be seen that this variable fluctuates between 5 and 9, showing noticeable short-term fluctuations with frequent rises and drops. Urban stations such as Guanyuan, Gucheng, and Nongzhanguan displayed slightly higher levels, likely influenced by heavier traffic and localized emission sources. In contrast, suburban sites such as Changping and Huairou tend to record lower concentrations.

Finally, in Table 1, we present summary statistics for the variables included in this dataset, namely $\log(\text{CO})$, temperature (TEMP, $^\circ\text{C}$), wind speed (WSP, m/s), and atmospheric pressure (PRES, Pa). These variables serve as suitable covariates for predicting CO concentrations.

Table 1: Beijing air pollutants data. Summary statistics of the variables of interest

Variable	Mean	Median	s.d	Min	Max
$\log(\text{CO})$ (response)	7.081	7.173	1.042	4.611	9.204
TEMP	-0.551	-0.503	3.992	-12.521	10.502
PRES	10.216	10.219	5.830	99.740	1036.00
WSP	1.643	1.304	1.202	0.000	9.600

3 The model

Consider the spatiotemporal Gaussian process $\{Y(s, t) : s \in \mathcal{S}, t \in \mathcal{T}\}$, where \mathcal{S} denotes a countable collection of spatial locations at which observations are available, \mathcal{T} represents a countable and ordered set of time points, and s and t index space and time, respectively.

The spatiotemporal model is then specified as,

$$Y(s_i, t_q) = \mu(s_i, t_q) + \omega(s_i, t_q) + \varepsilon_{iq}, \quad i = 1, \dots, n, \quad q = 1, \dots, T_i, \quad (1)$$

where n is the number of sites, T_i is the number of temporal replicates at site s_i and $N = \sum_{i=1}^n T_i$ is the total number of observations. In (1), the mean component is specified as $\mu(s_i, t_j) = \sum_{k=1}^p x_k(s_i, t_j) \beta_k$, where $x_1(s_i, t_j), \dots, x_p(s_i, t_j)$ are known covariates observed at (s_i, t_j) , and $(\beta_1, \dots, \beta_p)^\top$, is a vector of unknown regression coefficients to be estimated. The latent term $\omega(s_i, t_j)$ denotes the spatiotemporal random effect, with $\boldsymbol{\omega} = (\omega(s_1, t_1), \dots, \omega(s_1, t_{T_1}), \dots, \omega(s_n, t_1), \dots, \omega(s_n, t_{T_n}))$ assumed to follow a multivariate normal distribution with zero mean and covariance matrix \mathbf{C} . This component accounts for spatial and temporal dependence structures in the data. Finally, the measurement error is modeled as $\varepsilon_{iq} \sim \mathcal{N}(0, \tau^2)$, an independent Gaussian white-noise process capturing variability not explained by the structured spatiotemporal component.

Note that model (1) can be expressed in matrix form as

$$\mathbf{Y} = \mathbf{X}\boldsymbol{\beta} + \boldsymbol{\omega} + \boldsymbol{\varepsilon}, \quad (2)$$

where $\mathbf{Y} = (Y_{11}, \dots, Y_{nT_n})^\top$ with $Y_{iq} = Y(s_i, t_q)$, and \mathbf{X} is an $(N \times p)$ design matrix whose iq -th row is given by $\mathbf{x}_{iq}^\top = (x_{iq1}, \dots, x_{iqp})$, with $x_{iqk} = x_k(s_i, t_q)$. From the model specification, the latent random effects are distributed as $\boldsymbol{\omega} \sim \mathcal{N}_N(\mathbf{0}, \mathbf{C})$, and the error term as $\boldsymbol{\varepsilon} \sim \mathcal{N}_N(\mathbf{0}, \tau^2 \mathbf{I}_N)$, with $\boldsymbol{\varepsilon} = (\varepsilon_{11}, \dots, \varepsilon_{nT_n})^\top$, and \mathbf{I}_m denoting the $m \times m$ identity matrix. Consequently, the marginal distribution of \mathbf{Y} is an N -variate normal with

$$E(\mathbf{Y}) = \mathbf{X}\boldsymbol{\beta}, \quad \text{and} \quad \text{Var}(\mathbf{Y}) = \mathbf{C} + \tau^2 \mathbf{I}_N.$$

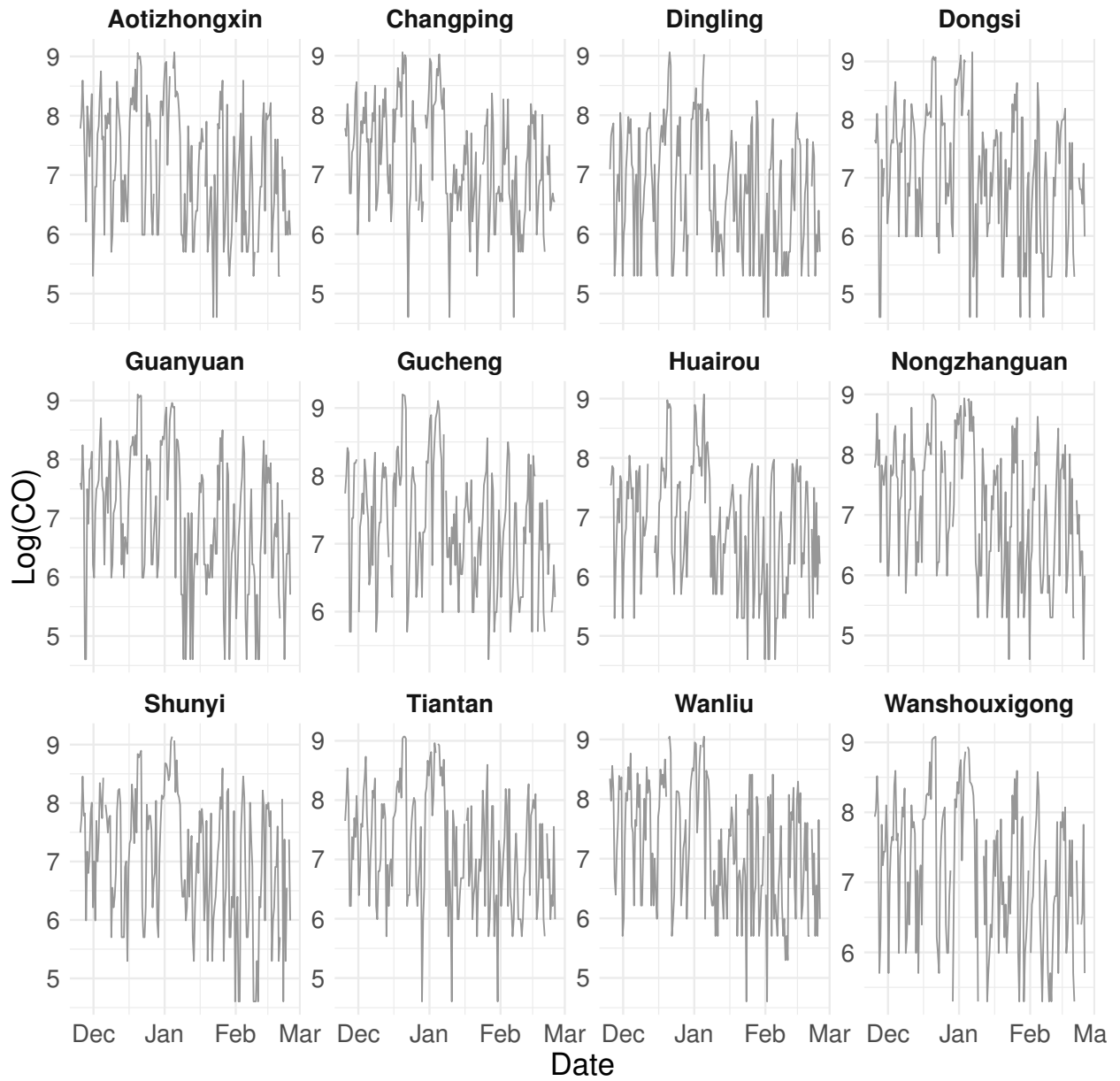


Figure 1: Time series of $\log(\text{CO})$ concentrations at twelve air-quality monitoring stations in Beijing from December to March.

In some situations, and depending on the measurement instrument, observations may be subject to upper and/or lower detection limits, beyond which they cannot be quantified. Additionally, missing data may occur for various reasons. For example, in the case of CO measurements, Kim et al. [12] reports that missingness can arise from instrument calibration and verification procedures, equipment malfunctions, repairs or replacements, and outlier removal during data preprocessing.

In the presence of censoring, the observed response Y_{iq} can be represented as (Z_{iq}, C_{iq}) , where Z_{iq} denotes either an uncensored observation, meaning that $Z_{iq} = Z_{iq0} = Y_{iq}$, or a detection limit corresponding to the censoring level when the observation is censored or missing. In the latter case, Z_{iq} takes the form $[Z_{iq1}, Z_{iq2}]$, indicating the interval within which the true value lies. C_{iq} , on the other hand, is the censoring indicator, defined as,

$$C_{iq} = \begin{cases} 1 & \text{if } Z_{iq1} \leq Y_{iq} \leq Z_{iq2}, \\ 0 & \text{if } Y_{iq} = Z_{iq0}. \end{cases} \quad (3)$$

As particular cases of (3), we have left censoring when $C_{iq} = 1$ and $Z_{iq} = [-\infty, Z_{iq2}]$, right censoring when $C_{iq} = 1$ and $Z_{iq} = [Z_{iq1}, \infty]$, and missingness when $C_{iq} = 1$ and $Z_{iq} = [-\infty, \infty]$. The model defined by (2) and (3) will be referred to as the normal spatio-temporal censored linear model over graphs (NST-CLG).

3.1 Specification of ω

We assume that $\omega \sim \mathcal{N}(\mathbf{0}, \mathbf{C})$ with a separable covariance structure

$$\mathbf{C} = \sigma^2(\Gamma \otimes \Phi),$$

where $\sigma^2 > 0$ is a variance (scale) parameter, Γ denotes the spatial correlation matrix, and Φ represents the temporal correlation matrix. The operator \otimes denotes the Kronecker product, which induces the separable spatiotemporal dependence structure.

3.1.1 Spatial correlation matrix Γ

Because our model is based on areal data, it is necessary to construct a correlation structure from a proximity matrix. In this context, the proximity matrix is defined through a graph representation, where the neighboring relationships between regions are encoded as edges connecting the corresponding vertices. In this setting, let $\mathcal{G} = \{\mathcal{S}, \mathcal{E}\}$ denote a graph with vertex set (regions) $\mathcal{S} = \{s_1, \dots, s_n\}$ and edge set $\mathcal{E} = \{(s_i, s_j) : s_i, s_j \in \mathcal{S}\}$, with cardinality $|\mathcal{E}| = n-1$. We write $s_i \sim s_j$ to indicate an edge connecting s_i and s_j . Therefore, we consider

$$\Gamma = [(\mathbf{I}_n - \mathbf{B}_n)^\top \mathbf{F}_n (\mathbf{I}_n - \mathbf{B}_n)]^{-1} \quad (4)$$

under two cases.

1. The first structure is based on the SAR model. In this setup, $\mathbf{F}_n = \kappa \mathbf{I}_n$, with $\kappa > 0$ is an unknown parameter which is fixed equal to 1 to avoid identifiability issues, and $\mathbf{B}_n = \rho \mathbf{A}_S$, with ρ a spatial autoregression parameter, and \mathbf{A}_S a $n \times n$ proximity matrix, with elements $a_{ij}^s = 1$ if $s_i \sim s_j$ and 0 elsewhere, for $i, j = 1, \dots, n$. As noted in Banerjee et al. [3], it is necessary to ensure the non-singularity of $(\mathbf{I} - \mathbf{B}_n)$ in order for Γ to define a valid (positive definite) covariance matrix. This can be achieved by setting $\rho \in (1/\lambda_{(1)}, 1/\lambda_{(n)})$, where $\lambda_{(1)} < \lambda_{(2)} < \dots < \lambda_{(n)}$ are the ordered eigenvalues of \mathbf{A}_S . Alternatively, \mathbf{A}_S can be replaced by the row stochastic matrix $\tilde{\mathbf{A}}_S = (\tilde{a}_{ij}^s)$, where $\tilde{a}_{ij}^s = a_{ij}^s / a_{i+}^s$ with $a_{i+}^s = \sum_j a_{ij}^s$. Redefining \mathbf{B}_n as $\alpha \tilde{\mathbf{A}}_S$, with α a spatial correlation parameter, the non-singularity condition is reduced to $\alpha \in (-1, 1)$ given that the eigenvalues of $\tilde{\mathbf{A}}_S$ are less or equal than one.
2. The second structure is based on the DAGAR model. Consider $N_S(s_i) = \{s_j : s_j \sim s_i, \text{ with } j < i\}$ as the set of neighbors of s_i . Define,

$$b_{ij} = \begin{cases} 0 & \text{for } j \text{ such that } s_j \notin N_S(s_i); \\ \frac{\rho}{1 + (n_{s_i} - 1)\rho^2} & \text{for } i = 2, \dots, n \text{ and } j \text{ such that } s_j \in N_S(s_i) \end{cases}$$

$$f_{ii} = \frac{1 + (n_{<i} - 1)\rho^2}{1 - \rho^2},$$

with a spatial correlation parameter $\rho > 0$, and n_{s_i} , the number of elements in $N_S(s_i)$. Here, the elements of the matrix \mathbf{B}_n are denoted by b_{ij} , and the matrix \mathbf{F}_n is diagonal with entries f_{ii} .

Note that we include only areal models whose covariance matrices can be expressed as in (4). The distributions of these models are induced through a noise term, analogous to the formulation of an autoregressive process of order p , $\text{AR}(p)$. In contrast, conditional autoregressive (CAR) models specify the distribution directly on the variable of interest, leading to a covariance structure that differs from that of the SAR and DAGAR models. As our analysis focuses exclusively on models of the form (4), the CAR specification is not considered further in this study.

3.1.2 Temporal correlation matrix Φ

In this setup, we assume that $T_i = T$ for all $i = 1, \dots, n$. For the temporal component Φ , we adopt a correlation structure induced by an autoregressive process of order p , denoted $\text{AR}(p)$. In this case, Φ takes the Toeplitz form

$$\Phi = \begin{bmatrix} \phi_0 & \phi_1 & \cdots & \phi_{T-1} \\ \phi_1 & \phi_0 & \cdots & \phi_{T-2} \\ \vdots & \vdots & \ddots & \vdots \\ \phi_{T-1} & \phi_{T-2} & \cdots & \phi_0 \end{bmatrix}, \quad (5)$$

where ϕ_k denotes the correlation at lag k . These correlations are determined by the Yule-Walker equations [4], $\phi_k = \gamma_1 \phi_{k-1} + \dots + \gamma_p \phi_{k-p}$, with $\gamma_1, \dots, \gamma_p$ representing the autoregressive parameters. For this process, the stationarity conditions depend on the roots of its characteristic polynomial $A(z) = 1 - \sum_{i=1}^p \gamma_i z^i$. The process is stationary if and only if all the roots of $A(z) = 0$ lie outside the unit circle in the complex plane. This condition guarantees that the process has a finite variance and an autocovariance function that depends only on the temporal lag rather than on the specific time index.

3.1.3 Innovation-form Gaussian Markov random field representation of ω

First, we introduce the following notations. For a fixed spatial location s_j , we define $\omega_{s_j} = (\omega(s_j, t_1), \dots, \omega(s_j, t_T))^\top$. Similarly, for a fixed time point t_j , with $t_1 < t_2 < \dots < t_k$, we denote $\omega_{t_j} = (\omega(s_1, t_j), \dots, \omega(s_n, t_j))^\top$. Note that this notation allows us to express the process as a Gaussian Markov random field in its innovation form (GMRFI), as follows:

$$\omega_{t_j} = \mathbf{B}_n \omega_{t_j} + \epsilon_{t_j}, \quad (6)$$

where $\epsilon_{t_j} = (\epsilon(s_1, t_j), \dots, \epsilon(s_n, t_j))^\top \sim \mathcal{N}_n(\mathbf{0}, \mathbf{F}_n)$.

The following results demonstrate that the Kronecker structure allows us to represent ω as a Gaussian Markov random field in its innovation form (GMRFI), which, through appropriate adjacency relations, captures both temporal and spatial dependencies. We begin by showing that when ω_{s_j} follows an $\text{AR}(p)$ structure, it admits such a representation. In particular, it can be expressed as a DAGAR process, where each coefficient b_{ij} is defined in terms of the parameters of the corresponding autoregressive polynomial.

Proposition 3.1. *Assuming an $\text{AR}(p)$ structure, the random effect ω_{s_j} follows a T -variate normal distribution with zero mean and covariance matrix given by*

$$[(\mathbf{I}_T - \mathbf{B}_T)^\top \mathbf{F}_T (\mathbf{I}_T - \mathbf{B}_T)]^{-1},$$

where \mathbf{B}_T has elements b_{ij} , with $i, j \in \{1, \dots, T\}$, given by

$$b_{ij} = \begin{cases} 0 & \text{for } t_j \notin N_{\mathcal{T}}(t_i); \\ \gamma_{i-j} & \text{for } i = 2, \dots, T \text{ and } t_j \in N_{\mathcal{T}}(t_i), \end{cases}$$

$N_{\mathcal{T}}(t_i) = (t_{i-1}, \dots, t_{i-p})$, and $\mathbf{F}_T = \sigma^{-2} \mathbf{I}_T$.

Proof: The proof of this proposition is provided in the Supplementary Material.

It is important to stress that the random effect ω_{s_j} admits a DAG representation, where the adjacency matrix is given by $\mathbf{A}_T = \sum_{k=1}^p \mathbf{J}^k$, with \mathbf{J}^k the k -th backward shift matrix, whose elements are $(\mathbf{J}^k)_{ij} = 1$ if $j = i - k$, and 0 otherwise. This matrix encodes a neighborhood structure by connecting each node t with its p predecessors $(t - k)$, allowing ω_{s_j} to be defined as an $\text{AR}(p)$ process. A graphical representation of this relationship is shown in Figure 2 for the cases $p = 1, 2$.

Next, we show that the random effect ω , under the specifications given above, can be expressed as a GMRFI, thus extending the SAR and DAGAR models to the spatiotemporal framework.

Theorem 3.1. *The process $\omega \sim \mathcal{N}_N(\mathbf{0}, \mathbf{C})$ can be written as a GMRFI process. Specifically,*

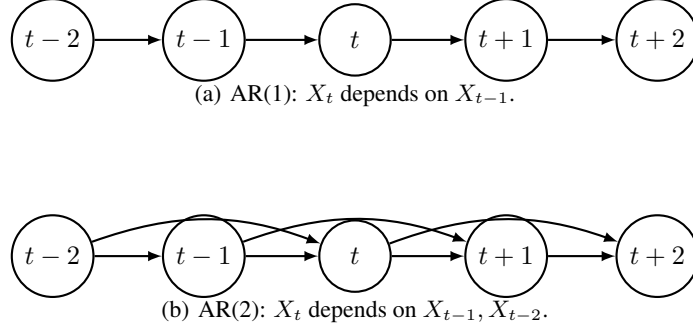


Figure 2: Directed acyclic graph representations of AR(1) and AR(2) processes.

1. Let $\mathbf{A} = \mathbf{I}_n \otimes \mathbf{A}_T + \mathbf{A}_S \otimes \mathbf{I}_T + \mathbf{A}_S \otimes \mathbf{A}_T$ denote the adjacency matrix, with elements $a_{(ik,jl)} = \delta_{ik}^S a_{jl}^T + a_{ik}^S \delta_{jl}^T + a_{ik}^S a_{jl}^T$, where $i, k \in \{1, \dots, n\}$, $j, l \in \{1, \dots, T\}$, and δ_{ik}^S and δ_{jl}^T are Kronecker delta functions representing the components of \mathbf{I}_n and \mathbf{I}_T , respectively. We define the following relationship: $(s_i, t_j) \sim (s_k, t_l)$ if $a_{(ik,jl)} = 1$. Note that the relation \sim defines a pair of neighbors in the spatiotemporal context. If Γ is chosen as the covariance matrix of a SAR process, then ω is a GMRFI with,

$$\omega(s_i, t_j) = \sum_{\{(s_k, t_l) : (s_i, t_j) \sim (s_k, t_l)\}} b_{(ik,jl)} \omega(s_k, t_l) + \epsilon(s_i, t_j) \quad (7)$$

where $\epsilon(s_i, t_j) \sim \mathcal{N}(0, \sigma^2 \mathbf{I})$ and

$$b_{(ik,jl)} = \begin{cases} 0 & \text{for } (s_i, t_j) \approx (s_k, t_l); \\ \gamma_{j-l} & \text{for } s_i = s_k \text{ and } t_l \in N_{\mathcal{T}}(t_j), \\ \tilde{a}_{ik}^s \rho & \text{for } t_j = t_l \text{ and } s_i \sim s_k, \\ -\tilde{a}_{ik}^s \rho \gamma_{j-l} & \text{for } s_i \sim s_k, t_l \in N_{\mathcal{T}}(t_j), i \neq k, j \neq l \end{cases}$$

with \tilde{a}_{ik}^s being the element (i, k) of the matrix $\tilde{\mathbf{A}}_S$ as defined in Section 3.1.1.

2. If Γ is chosen as the covariance structure of a DAGAR process, then ω is also a DAGAR process, i.e.,

$$\omega(s_1, t_1) = \epsilon(s_1, t_1) \quad (8)$$

$$\omega(s_i, t_j) = \sum_{\mathcal{C}} b_{(ik,jl)} \omega(s_k, t_l) + \epsilon(s_i, t_j) \quad (9)$$

where $\mathcal{C} = \{(s_k, t_l) : (s_k, t_l) \in N_{(\mathcal{S}, \mathcal{T})}\}$, $\epsilon(s_i, t_j) \sim \mathcal{N}(0, f_{ii}^{-1} \sigma^2)$, $N_{(\mathcal{S}, \mathcal{T})}(s_i, t_j) = N_{\mathcal{S}}(s_i) \times N_{\mathcal{T}}(t_j)$ and

$$b_{(ik,jl)} = \begin{cases} 0 & \text{for } (s_k, t_l) \notin N_{\mathcal{S}, \mathcal{T}}(s_i, t_j); \\ \gamma_{j-l} & \text{for } s_i = s_k \text{ and } t_l \in N_{\mathcal{T}}(t_j), \\ \frac{\rho}{1+(n_{<i}-1)\rho^2} & \text{for } t_i = t_j \text{ and } s_k \in N_{\mathcal{S}}(s_i), \\ -\frac{\rho}{1+(n_{<i}-1)\rho^2} \gamma_{j-l} & \text{for } s_k \in N_{\mathcal{S}}(s_i), t_l \in N_{\mathcal{T}}(t_j), k \neq i, l \neq j \end{cases}$$

Proof: The proof is provided in the Supplementary Material.

In the first statement of Theorem 3.1, the choice of \tilde{a}_{ik}^s is made purely for convenience when verifying the nonsingularity of the matrix $(\mathbf{I}_n - \mathbf{B}_n)$. The statements continue to hold if a_{ik}^s , the (i, k) -th element of the matrix \mathbf{A}_S , is used instead of \tilde{a}_{ik}^s . Using Γ as the SAR covariance structure, (7) allows us to rewrite the process as

$$\begin{aligned} \omega(s_i, t_j) &= \underbrace{\sum_{q=1}^p \gamma_q \omega(s_i, t_{j-q})}_{\mathbb{A}} + \underbrace{\sum_{k \neq i} \tilde{a}_{ik}^s \rho \omega(s_k, t_j)}_{\mathbb{B}} \\ &- \underbrace{\sum_{k \neq i} \sum_{q=1}^p \tilde{a}_{ik}^s \gamma_q \rho \omega(s_k, t_{j-q})}_{\mathbb{C}} + \epsilon(s_i, t_j). \end{aligned} \quad (10)$$

On the other hand, using Γ as the DAGAR covariance structure, equations (8)-(9) allow us to rewrite the process as

$$\begin{aligned} \omega(s_i, t_j) &= \underbrace{\sum_{q=1}^p \gamma_q \omega(s_i, t_{j-q})}_{\mathbb{A}} + \underbrace{\sum_{s_k \in \mathcal{N}_{\mathcal{S}}(s_i)} \frac{\rho}{1 + (n_{s_i} - 1)\rho^2} \omega(s_k, t_j)}_{\mathbb{B}} \\ &- \underbrace{\sum_{s_k \in \mathcal{N}_{\mathcal{S}}(s_i)} \sum_{q=1}^p \frac{\gamma_q \rho}{1 + (n_{s_i} - 1)\rho^2} \omega(s_k, t_{j-q})}_{\mathbb{C}} + \epsilon(s_i, t_j) \end{aligned} \quad (11)$$

Regarding equation (10), γ_q in component \mathbb{A} denotes the autoregressive parameter for the fixed location s_i . Moreover, in component \mathbb{B} , the parameter ρ , which is associated with spatial correlation, poses interpretational challenges similar to those documented for SAR models at a fixed time point [see 3, 19]. Note that component \mathbb{C} incorporates both spatial and temporal parameters. However, the process form in (11) provides a more direct interpretation of the spatial and temporal parameters and their interactions, with the advantage that both parameters can be interpreted analogously to those in AR(p) and DAGAR models. The component \mathbb{A} captures temporal dependence. Marginally, the coefficients γ_q can be interpreted as the conditional linear effect of $\omega(s_i, t_{j-q})$ on the current value $\omega(s_i, t_j)$, holding the remaining lags constant. The component \mathbb{B} captures spatial dependence, where ρ can be interpreted marginally as the correlation between $\omega(s_i, t_j)$ and its spatial neighbors. Finally, the term \mathbb{C} accounts for the spatiotemporal cross-dependence, and the product $\gamma_q \rho$ can be interpreted as a measure of dependence between $\omega(s_i, t_j)$ and the past values of its spatial neighbors.

It is worth noting that, as in the purely spatial DAGAR model, the assumptions regarding ordering rely solely on the spatial dimension. Following Datta et al. [8], let $\pi = \pi(1), \dots, \pi(n)$ denote any predetermined ordering of the spatial locations, and let π^{-1} be its corresponding inverse permutation. Under this ordering, for $i \neq \pi(1)$, define the set of neighboring observations $\omega_{N_{\mathcal{S}}(s_i)}$ as the collection $\{\omega(s_k, t_l) : \pi^{-1}(k) < \pi^{-1}(i), t_l \in N_{\mathcal{T}}(t_j)\}$, where $N_{\mathcal{S}}^{\pi}(s_i) = \{s_k : s_i \sim s_k, \pi^{-1}(k) < \pi^{-1}(i)\}$. Denote by $\mathcal{G}_{\pi}(\mathcal{S}, \mathcal{E}_{\pi})$ the acyclic graph generated by these configurations, with \mathcal{E}_{π} representing the collection of directed edges from all members of $N_{\mathcal{S}}^{\pi}(s_i)$ to i , for every $i \neq \pi(1)$. Then,

$$\omega(s_i, t_j) \mid \omega_{N_{(\mathcal{S}, \mathcal{T})}^{\pi}(s_i, t_j)} \sim \mathcal{N} \left(\sum_{(s_k, t_l) \in N_{(\mathcal{S}, \mathcal{T})}^{\pi}(s_i, t_j)} b_{(ik, jl)} \omega(s_k, t_l), f_{ii}^{-1} \sigma^2 \right),$$

with $N_{(\mathcal{S}, \mathcal{T})}^{\pi}(s_i, t_j) = N_{\mathcal{S}}^{\pi}(s_i) \times N_{\mathcal{T}}(t_j)$ and $b_{(ik, jl)}$ as defined in Theorem 3.1, but replacing n_{s_i} by $n_{\pi(i)}$, the number of elements in $N_{\mathcal{S}}^{\pi}(s_i)$. It is worth noting that Datta et al. [8] reported that the ordering of regions has a negligible influence on the results. Specifically, in their simulation studies, the mean squared errors, as well as the estimates and credible intervals for ρ , remained nearly identical across different orders.

4 Bayesian inference

To perform Bayesian inference for the NST-CLG model, we treat the censored responses \mathbf{Y}^c as latent variables and target the joint posterior $\pi(\boldsymbol{\beta}, \sigma^2, \rho, \psi, \boldsymbol{\gamma}, \mathbf{Y}^c \mid \mathbf{y}^o)$. We first translate the results of Berger et al. [5] into the context of regression models defined over graphs. Denote $\boldsymbol{\beta} = (\beta_0, \dots, \beta_p)$ and $\boldsymbol{\gamma} = (\gamma_1, \dots, \gamma_p)^{\top}$, and assume that

$$\pi(\boldsymbol{\beta}, \sigma^2, \rho, \psi, \boldsymbol{\gamma}) \propto \frac{\pi(\rho, \psi, \boldsymbol{\gamma})}{\sigma^2}, \quad (12)$$

We then obtain the following result for the augmented-data posterior distribution $\pi(\rho, \psi, \boldsymbol{\gamma} \mid \mathbf{y})$ under an arbitrary prior $\pi(\rho, \psi, \boldsymbol{\gamma})$.

Proposition 4.1. *Let $\text{Cov}(\mathbf{Y}) = \boldsymbol{\Sigma} = \sigma^2(\Gamma \otimes \Phi + \psi \mathbf{I})$, where $\psi = \tau^2/\sigma^2$. Then, given the data augmented-data $\mathbf{y} = \text{vec}(\mathbf{y}^o, \mathbf{y}^c)$, and a prior density $\pi(\rho, \psi, \boldsymbol{\gamma})$, the posterior $\pi(\rho, \psi, \boldsymbol{\gamma} \mid \mathbf{y})$ can be written as,*

$$\pi(\rho, \psi, \boldsymbol{\gamma} \mid \mathbf{y}) \propto |\boldsymbol{\Sigma}|^{-1/2} \left| V_{\hat{\boldsymbol{\beta}}} \right|^{1/2} (S^2)^{-N-p/2} \pi(\rho, \psi, \boldsymbol{\gamma}), \quad (13)$$

where $S^2 = (\mathbf{y} - \mathbf{X}\hat{\boldsymbol{\beta}})^{\top} \boldsymbol{\Sigma}^{-1} (\mathbf{y} - \mathbf{X}\hat{\boldsymbol{\beta}}) / N-p$, $V_{\hat{\boldsymbol{\beta}}} = (\mathbf{X}^{\top} \boldsymbol{\Sigma}^{-1} \mathbf{X})^{-1}$, and $\hat{\boldsymbol{\beta}} = (\mathbf{X}^{\top} \boldsymbol{\Sigma}^{-1} \mathbf{X})^{-1} \mathbf{X}^{\top} \mathbf{y}$ is the least square estimator of $\boldsymbol{\beta}$.

A proof of this result can be found in the Supplementary Material. Because of standard properties of the multivariate normal distribution, together with the prior specification in (12), we also have

$$\pi(\boldsymbol{\beta}, \sigma^2 \mid \rho, \psi, \boldsymbol{\gamma}, \mathbf{y}) \propto \frac{1}{|V_{\hat{\boldsymbol{\beta}}}|^{1/2}} \exp \left[\frac{(\boldsymbol{\beta} - \hat{\boldsymbol{\beta}})^\top V_{\hat{\boldsymbol{\beta}}}^{-1} (\boldsymbol{\beta} - \hat{\boldsymbol{\beta}})}{2\sigma^2} \right] \times \\ (S^2)^{N-p/2} (\sigma^2)^{-(N-p/2+1)} \exp \left\{ -\frac{(N-p)S^2}{2\sigma^2} \right\}. \quad (14)$$

Consider reordering the vector \mathbf{Y} such that it can be expressed as $\mathbf{Y} = \text{vec}(\mathbf{Y}^o, \mathbf{Y}^c)$, where $\text{vec}(\cdot)$ denotes the function that stacks vectors or matrices having the same number of columns, \mathbf{Y}^o is the N^o -dimensional vector of observed responses, \mathbf{Y}^c is the N^c -dimensional vector of censored/missing observations, and $N = N^o + N^c$. As with the response, consider the reorderings

$$\mathbf{X}^\top = [\mathbf{X}^{o\top} \quad \mathbf{X}^{c\top}], \quad \mathbf{Z}^\top = [\mathbf{Z}^{o\top} \quad \mathbf{Z}^{c\top}], \quad \boldsymbol{\mu} = \begin{bmatrix} \mathbf{X}^o \boldsymbol{\beta} \\ \mathbf{X}^c \boldsymbol{\beta} \end{bmatrix}, \quad \boldsymbol{\Sigma} = \begin{bmatrix} \boldsymbol{\Sigma}^{oo} & \boldsymbol{\Sigma}^{oc} \\ \boldsymbol{\Sigma}^{co} & \boldsymbol{\Sigma}^{cc} \end{bmatrix},$$

with $\boldsymbol{\Sigma} = \mathbf{C} + \tau^2 \mathbf{I}_N$. Given standard properties of the multivariate normal distribution, it follows that $\mathbf{Y}^o \sim \mathcal{N}_{N^o}(\mathbf{X}^o \boldsymbol{\beta}, \boldsymbol{\Sigma}^{oo})$ and $\mathbf{Y}^c \mid \mathbf{Y}^o \sim \mathcal{N}_{N^c}(\boldsymbol{\mu}^{c|o}, \boldsymbol{\Sigma}^{c|o})$, where $\boldsymbol{\mu}^{c|o} = \mathbf{X}^c \boldsymbol{\beta} + \boldsymbol{\Sigma}^{co}(\boldsymbol{\Sigma}^{oo})^{-1}(\mathbf{Y}^o - \mathbf{X}^o \boldsymbol{\beta})$, $\boldsymbol{\Sigma}^{c|o} = \boldsymbol{\Sigma}^{cc} - \boldsymbol{\Sigma}^{co}(\boldsymbol{\Sigma}^{oo})^{-1}\boldsymbol{\Sigma}^{oc}$. Using the results above, the full conditional distribution of \mathbf{Y}^c is a multivariate truncated normal distribution, that is,

$$\mathbf{Y}^c \mid \mathbf{y}^o, \boldsymbol{\beta}, \sigma^2, \rho, \psi, \boldsymbol{\gamma} \sim \mathcal{TN}_{N^c}(\boldsymbol{\mu}^{c|o}, \boldsymbol{\Sigma}^{c|o}, \mathbb{Z}^c),$$

where

$$\mathbb{Z}^c = \left\{ \mathbf{Y}^c = (Y_{11}^c, \dots, Y_{ij}^c)^\top \mid Z_{111}^c \leq Y_{11}^c \leq Z_{112}^c, \dots, Z_{ij1}^c \leq Y_{ij}^c \leq Z_{ij2}^c \right\}$$

and $P(\mathbf{u} \in \mathbb{Z}^c \mid \mathbf{Y}^o)$ is the conditional probability that \mathbf{u} belongs in the set \mathbb{Z}^c given the observed response.

For a given vector \mathbf{y}^c , we have $\boldsymbol{\beta} \mid \rho, \boldsymbol{\gamma}, \mathbf{y} \sim N_p(\hat{\boldsymbol{\beta}}, V_{\hat{\boldsymbol{\beta}}})$ and $\sigma^2 \mid \rho, \psi, \boldsymbol{\gamma}, \mathbf{y} \sim \chi_{ScI}^2(N-p, S^2)$, that is, the scale inverse chi-square distribution. Based on these results, we propose a Gibbs sampler in which the sampled \mathbf{y}^c and (13) are used in a Metropolis step to obtain samples from $\pi(\rho, \boldsymbol{\gamma} \mid \mathbf{y})$. Subsequently, (14) is used to generate samples from the full conditional posteriors $\boldsymbol{\beta} \mid \rho, \psi, \boldsymbol{\gamma}, \mathbf{y}$ and $\sigma^2 \mid \rho, \psi, \boldsymbol{\gamma}, \mathbf{y}$. These steps are summarized in Algorithm 1.

Algorithm 1 Posterior Sampling Algorithm for the NST-CLG Model

1: Sample $(\rho^{(s)}, \psi^{(s)}, \boldsymbol{\gamma}^{(s)})$:

- Initialize the parameters $(\rho^{(0)}, \psi^{(0)}, \boldsymbol{\gamma}^{(0)})$ and $\mathbf{y}^{c(0)}$. Form the vector $\mathbf{y}^{(0)} = (\mathbf{y}^o, \mathbf{y}^{c(0)})$
- Generate a candidate $(\rho^*, \psi^*, \boldsymbol{\gamma}^*)$ from an independent proposal $q(\rho, \psi, \boldsymbol{\gamma}) = q(\rho)q(\boldsymbol{\gamma})q(\psi)$.
- Calculate $M = \frac{\pi(\rho^*, \psi^*, \boldsymbol{\gamma}^* \mid \mathbf{y}^{(s-1)})q(\rho^{(s-1)}, \psi^{(s-1)}, \boldsymbol{\gamma}^{(s-1)})}{\pi(\rho^{(s-1)}, \psi^{(s-1)}, \boldsymbol{\gamma}^{(s-1)} \mid \mathbf{y}^{(s-1)})q(\rho^*, \psi^*, \boldsymbol{\gamma}^*)}$.
- Sample $U \sim \text{Uniform}(0, 1)$.
- Set $(\rho^{(s)}, \psi^{(s)}, \boldsymbol{\gamma}^{(s)}) = (\rho^*, \psi^*, \boldsymbol{\gamma}^*)$ if $u < M$ or $(\rho^{(s)}, \psi^{(s)}, \boldsymbol{\gamma}^{(s)}) = (\rho^{(s-1)}, \psi^{(s-1)}, \boldsymbol{\gamma}^{(s-1)})$ otherwise.

2: Sample $\sigma^{2(s)} \sim \chi_{ScI}^2(N-p, S^2)$, with $S^2 = S^2(\rho^{(s)}, \psi^{(s)}, \boldsymbol{\gamma}^{(s)})$ as in Proposition 3.1. Recover $\tau^{2(s)} = \sigma^{2(s)}\psi^{(s)}$.

3: Sample $\boldsymbol{\beta}^{(s)} \sim N_p(\hat{\boldsymbol{\beta}}, V_{\hat{\boldsymbol{\beta}}})$ with $\hat{\boldsymbol{\beta}} = \hat{\boldsymbol{\beta}}(\rho^{(s)}, \psi^{(s)}, \boldsymbol{\gamma}^{(s)})$ and $V_{\boldsymbol{\beta}} = V_{\boldsymbol{\beta}}(\rho^{(s)}, \psi^{(s)}, \boldsymbol{\gamma}^{(s)})$ as in Proposition 3.1.

4: Sample $\mathbf{Y}^{c(s)} \mid \mathbf{Y}^o, \boldsymbol{\beta}^{(s)}, \sigma^{2(s)}, \rho^{(s)}, \psi^{(s)}, \boldsymbol{\gamma}^{(s)} \sim \mathcal{TN}_{N^c}(\boldsymbol{\mu}^{c|o}, \boldsymbol{\Sigma}^{c|o}, \mathbb{Z})$ with $\boldsymbol{\mu}^{c|o} = \boldsymbol{\mu}^{c|o}(\boldsymbol{\beta}^{(s)}, \sigma^{2(s)}, \rho^{(s)}, \psi^{(s)}, \boldsymbol{\gamma}^{(s)})$ and $\boldsymbol{\Sigma}^{c|o} = \boldsymbol{\Sigma}^{c|o}(\boldsymbol{\beta}^{(s)}, \sigma^{2(s)}, \rho^{(s)}, \psi^{(s)}, \boldsymbol{\gamma}^{(s)})$ as defined earlier.

4.1 Specification of $\pi(\rho, \psi, \boldsymbol{\gamma})$

We assume an independent joint prior of the form

$$\pi(\rho, \psi, \boldsymbol{\gamma}) \propto \pi(\rho)\pi(\psi)\pi(\boldsymbol{\gamma}), \quad (15)$$

where $\rho \sim \text{Beta}(a_\rho, b_\rho)$, $\psi \sim \text{Beta}(a_\psi, b_\psi)$, and $\boldsymbol{\gamma} \sim \text{Beta}(a_\boldsymbol{\gamma}, b_\boldsymbol{\gamma})$. The beta distribution is a convenient choice due to its flexibility and computational advantages. Its support on a bounded interval ensures coherence with the parameter space. In contrast, its shape parameters (a, b) allow a wide range of prior specifications, from uniform to highly concentrated forms.

4.2 Bayesian prediction

Let s_i be a fixed location, $\tilde{T} = (\tilde{t}_1, \tilde{t}_2, \dots, \tilde{t}_{n_{pred}})$ be a set of times for predicting the response $Y(s_i, t)$, and $\boldsymbol{\theta} = (\beta, \sigma^2, \rho, \psi, \gamma)$. Denote \mathbf{Y}^{pred} as the $N_{pred} \times 1$ random vector with j th component $Y(s_i, \tilde{t}_j)$. Then, the posterior density of $(\mathbf{Y}^{pred}, \boldsymbol{\theta}, \mathbf{Y}^c)$ can be written as,

$$P(\mathbf{Y}^{pred}, \boldsymbol{\theta}, \mathbf{Y}^c | \mathbf{y}^o) = P(\boldsymbol{\theta}, \mathbf{Y}^c | \mathbf{y}^o)P(\mathbf{Y}^{pred} | \boldsymbol{\theta}, \mathbf{Y}^c, \mathbf{y}^o). \quad (16)$$

To get the predictive distribution $P(\mathbf{Y}^{pred} | \boldsymbol{\theta}, \mathbf{Y}^c, \mathbf{y}^o)$, we can use the results of Section 4. Let $\mathbf{Y}^* = \text{vec}(\mathbf{Y}^{obs}, \mathbf{Y}^{pred})$, where $\mathbf{Y}^{obs} = (\mathbf{Y}^o, \mathbf{Y}^c)$ and $\mathbf{X}^* = (\mathbf{X}, \tilde{\mathbf{X}})$ with $\tilde{\mathbf{X}}$, the covariates matrix associated to the values we want to predict. Then $\mathbf{Y}^* | \boldsymbol{\theta} \sim \mathcal{N}_{N+N_{pred}}(\boldsymbol{\mu}^*, \boldsymbol{\Sigma}^*)$, with,

$$\boldsymbol{\mu}^* = [\mathbf{X}^{obs}\boldsymbol{\beta} \quad \mathbf{X}^{pred}\boldsymbol{\beta}], \quad \boldsymbol{\Sigma} = \begin{bmatrix} \boldsymbol{\Sigma}^{obsobs} & \boldsymbol{\Sigma}^{obspred} \\ \boldsymbol{\Sigma}^{predobs} & \boldsymbol{\Sigma}^{predpred} \end{bmatrix},$$

and $\mathbf{Y}^{pred} | \mathbf{Y}^{obs}, \boldsymbol{\theta} \sim \mathcal{N}_{N_{pred}}(\boldsymbol{\mu}^{pred|obs}, \boldsymbol{\Sigma}^{pred|obs})$, where

$$\begin{aligned} \boldsymbol{\mu}^{pred|obs} &= \mathbf{X}^{pred}\boldsymbol{\beta} + \boldsymbol{\Sigma}^{predobs} (\boldsymbol{\Sigma}^{obsobs})^{-1} (\mathbf{Y}^{obs} - \mathbf{X}^{obs}\boldsymbol{\beta}), \\ \boldsymbol{\Sigma}^{pred|obs} &= \boldsymbol{\Sigma}^{predpred} - \boldsymbol{\Sigma}^{predobs} (\boldsymbol{\Sigma}^{obsobs})^{-1} \boldsymbol{\Sigma}^{obspred} \end{aligned}$$

Similar to Banerjee [2], to sample from (16) we first obtain a sample from $\pi(\boldsymbol{\theta}, \mathbf{Y}^c | \mathbf{y}^o)$ using Algorithm 1. For each draw of $(\boldsymbol{\theta}, \mathbf{Y}^c)$, we generate a draw of the $N_{pred} \times 1$ vector \mathbf{Y}^{pred} from $P(\mathbf{Y}^{pred} | \boldsymbol{\theta}, \mathbf{Y}^c, \mathbf{y}^o)$. By computing summary measures such as the sample mean, median, or the 2.5% and 97.5% quantiles, we obtain posterior predictive inference for new values, conditional on the observed data and censoring information.

5 Simulation studies

In this section, we present two simulation studies. The first examines how censoring and missingness affect model fitting and demonstrates that our method accommodates them effectively. The second evaluates the out-of-sample predictive performance for future time points. To simulate the datasets, we independently generated $x_{1ij} \sim N(0, 1^2)$ and $x_{2ij} \sim N(1, 3^2)$, considering $\boldsymbol{\beta} = (1, 2, 2.5)^\top$ and $(\sigma^2, \rho, \gamma, \tau^2) = (2, 0.8, 0.7, 0.6)$. Using these values, we compute the linear predictor $\mathbf{X}\boldsymbol{\beta}$ and the spatiotemporal covariance matrix \mathbf{C} as specified in Section 3, for both the DAGAR and SAR processes. Finally, we simulate the response $\mathbf{Y} \sim \mathcal{N}_N(\mathbf{X}\boldsymbol{\beta}, \mathbf{C})$. In total, $k = 300$ datasets were simulated for each study. After simulating the data, $\delta\%$ of the values were artificially left censored, as in Schelin and de Luna [16]. We also generated missing values from the remaining $100 - \delta\%$ uncensored observations. The percentages of censored values were fixed at 15% and 35%, whereas the percentage of missing values was fixed at 5%. For comparison purposes, we compared our proposed approach with common techniques for dealing with partial information. The first method, the LOD method, consists of substituting the censored values with the limit of detection, whereas the second method, the LOD/2 method, substitutes these values with 0.5LOD. The missing values in these two methods were substituted by the sample mean of all the observations.

5.1 Simulation study I: Parameter estimation and model fitting

As mentioned above, our goal is to assess model fitting in the presence of censoring and missingness. In this case, we simulate the spatial structure using grids of sizes 3, 4, and 5, resulting in a total of $n_1 = 9$, $n_2 = 16$, and $n_3 = 25$ vertices (regions), respectively. When estimating both the spatial and temporal structures, we simulate the latter, considering the number of temporal observations to be the same as the number of regions, that is, $T_1 = 9$, $T_2 = 16$, $T_3 = 25$. This gives us the total number of observations of $N_i = n_i \times T_i$ for $i = 1, 2, 3$.

Regarding the comparison criteria, we calculated (i) the length of the 95% credible interval and (ii) the coverage probability for each parameter. The first was computed as the difference between the upper and lower credible interval limits for each simulation; these limits were obtained as the 2.5% and 97.5% percentiles of the posterior distribution sample in each simulation. The second was computed as the proportion of simulations in which the true parameter was within the credible interval limits. Concerning the DAGAR correlation, Figure 3 and Table 2 present the distribution of the 300 interval lengths and coverage probabilities for the variance structure parameters obtained using the NST-CLG

model, LOD, and LOD/2 methods under a censoring level of 15% and a missingness rate of 5%. The corresponding distribution of the interval lengths for the mean structural parameters is shown in Figure S.4.1 of the Supplementary Material. Additional results for the mean and covariance parameters under 35% censoring and 5% missingness are provided in Figures S.4.2 and S.4.3, as well as in Tables S.4.1, S.4.2, and S.4.3 of the Supplementary Material. With respect to the SAR process, Tables S.4.4 and S.4.5, and Figures S.4.4 and S.4.6 of the Supplementary Material show the distribution of lengths and coverage probabilities for the mean parameters under both censoring scenarios. On the other hand, Tables S.4.6 and S.4.7, and Figures S.4.5 and S.4.7 of the Supplementary Material, show these measures for the covariance parameters.

For the regression coefficients β , when censoring/missingness is 15/5%, the NST-CLG model yields the shortest posterior intervals with empirical coverage close to the nominal 95% level for all sample sizes, and the same pattern holds at censoring/missing levels of 35/5%. This behavior is expected; the proposed model accounts for censored values through an appropriate truncated likelihood. In contrast, the credible intervals given by the LOD and LOD/2 substitutions narrow as n increases, yet exhibit declining coverage. Constant replacements at the detection limit (or its half) and mean imputation for missingness shift the conditional mean and compress the residual spread, producing attenuation. As the sample size increases, the posterior concentrates around this biased center, so intervals become too tight and miss the target more often.

This pattern is consistent with covariance components. With 15% censoring and 5% missingness, the NST-CLG model produces the shortest posterior intervals and coverage closest to the nominal 95% for all the parameters and sample sizes. When censoring/missingness increases to 35%/40%, the intervals widen as expected, but the ranking does not change, and the NST-CLG model remains the best approach, while LOD and LOD/2 continue to under-cover. Similar results were observed for the SAR process, excepting for the intercept β_0 where the NST-CLG model presents slightly larger interval lengths but still, better coverage probabilities.

Table 2: Simulation study I. Coverage probabilities of the covariance structure parameters considering a level of censoring of 15%

N	Parameter	NST-CLG	LOD	LOD/2
81	σ^2	0.997	0.253	0.093
	ρ	0.997	0.990	0.990
	τ^2	0.980	0.9930	0.963
	γ	0.888	0.987	0.993
256	σ^2	1.000	0.080	0.053
	ρ	0.973	0.963	0.963
	τ^2	0.930	0.863	0.800
	γ	0.923	0.880	0.910
625	σ^2	0.990	0.110	0.063
	ρ	0.993	0.767	0.767
	τ^2	0.947	0.670	0.553
	γ	0.967	0.860	0.903

5.2 Simulation study II: Predictive performance in time domain

In this study, we evaluate the prediction performance of our method by comparing it with the traditional imputation techniques used in Subsection 5.1. For this purpose, we first simulated a spatiotemporal Gaussian process considering both DAGAR and SAR structures. We used a fixed grid of size 5 (25 regions), varying the temporal observations to $T_1 = 17$, $T_2 = 27$ and $T_3 = 37$, leaving $T_{est,i} = 10, 20, 30$, $i = 1, 2, 3$ temporal data points to estimate the process and use the remaining observations to assess the performance of our prediction proposal. The total number of observations considered for the estimation will then be $N_i = 250, 500, 750$ for $i = 1, 2, 3$ respectively. We considered the model parameters and levels of censoring/missingness to be the same as in Subsection 5.1.

With respect to the comparison criteria, we consider (i) the squared root of the mean square prediction error (MSPE), which, following the notation of Subsection 4.2 and for fixed regions s_1, \dots, s_K , $K \leq n$, is computed as,

$$\sqrt{\text{MSPE}} = \sqrt{\frac{1}{K * n_{pred}} \sum_{i=1}^K \sum_{\tilde{t}_j \in \tilde{T}} \left\{ \tilde{Y}(s_i, \tilde{t}_j) - Y(s_i, \tilde{t}_j) \right\}^2},$$

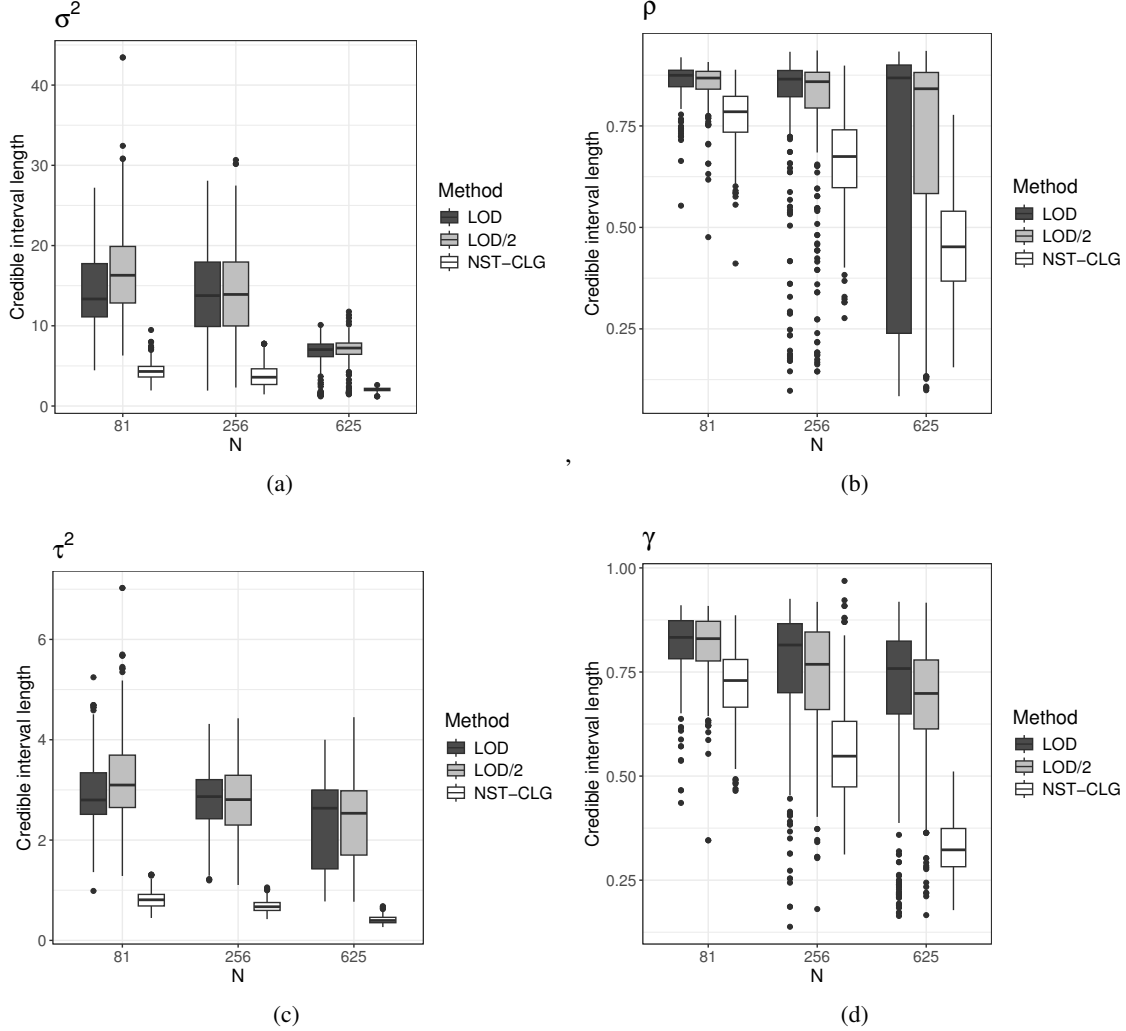


Figure 3: Simulation study I. Credible interval lengths for the covariance structure parameters considering a censoring level of 15% and a missing level of 5%

(ii) mean lengths of the 95% posterior predictive credible intervals for all predicted values. For each predicted value, this quantity is computed by obtaining the credible interval limits as the 2.5% and 97.5% percentiles of its predictive posterior distribution sample, and then calculating the interval length as the difference between the upper and lower credible interval limits for each simulation. We then computed the mean of the interval lengths across all predictions. Finally, we compute (iii) the mean coverage probability for all predictions. This measure was computed by obtaining the proportion of simulations in which each real value $Y(s_i, t_j)$ lies inside its credible interval limits, and then computing the mean of these proportions over all the predicted values.

For this simulation study, we created three scenarios by computing all the comparison criteria for one-, three-, and seven-step-ahead predictions. Regarding the DAGAR model, Figure 4 and Table 3 show the results for $N = 500$ and both censoring levels. The results for $N = 250$ and $N = 750$ are presented in Tables S.4.8 and S.4.9 and Figures S.4.8 and S.4.9 of the Supplementary Material. On the other hand, Figures S.4.10 - S.4.12 and Tables S.4.10 - S.4.12 show the simulation results for the SAR correlation.

With respect to the DAGAR model, the $\sqrt{\text{MSPE}}$ for the LOD method was the worst across all sample sizes, censoring levels, and prediction settings. The NST-CLG model and LOD/2 are broadly similar, with the former being slightly better. The gap is larger for the prediction-interval length: the NST-CLG model produces the narrowest intervals, while LOD yields the widest. Moreover, LOD/2 returns coverage near 1.0 in every setting, indicating overly wide intervals. The LOD improved as the sample size approached the 95% target at $N = 750$, after under- or overshooting

at smaller sample sizes. By contrast, our model stays close to 95% across all sample sizes, censoring levels, and prediction scenarios. Overall, the NST-CLG model delivers the best balance, with the smallest $\sqrt{\text{MSPE}}$ and shortest intervals, while maintaining coverage near the nominal 95% level. Regarding the SAR model, all three methods yield comparable $\sqrt{\text{MSPE}}$ values at the 15% and 5% levels of censoring and missingness, across all sample sizes. However, when the proportion of censored data increases to 35% (keeping a 5% proportion of missingness), the performance of the LOD approach deteriorates noticeably, whereas LOD/2 and our approach exhibit similar behavior, with the NST-CLG model performing slightly better overall. Regarding credible interval lengths and coverage probabilities, the LOD/2 method produces wider credible intervals but achieves coverage probabilities close to the nominal 95% level across all sample sizes. In contrast, the LOD method provides intervals of similar width to those of the NST-CLG model, but its coverage probabilities remain noticeably lower than the 95% nominal level. On the other hand, our proposed model maintains shorter intervals while still achieving coverage rates near the nominal level, demonstrating a clear advantage over the two ad hoc methods.

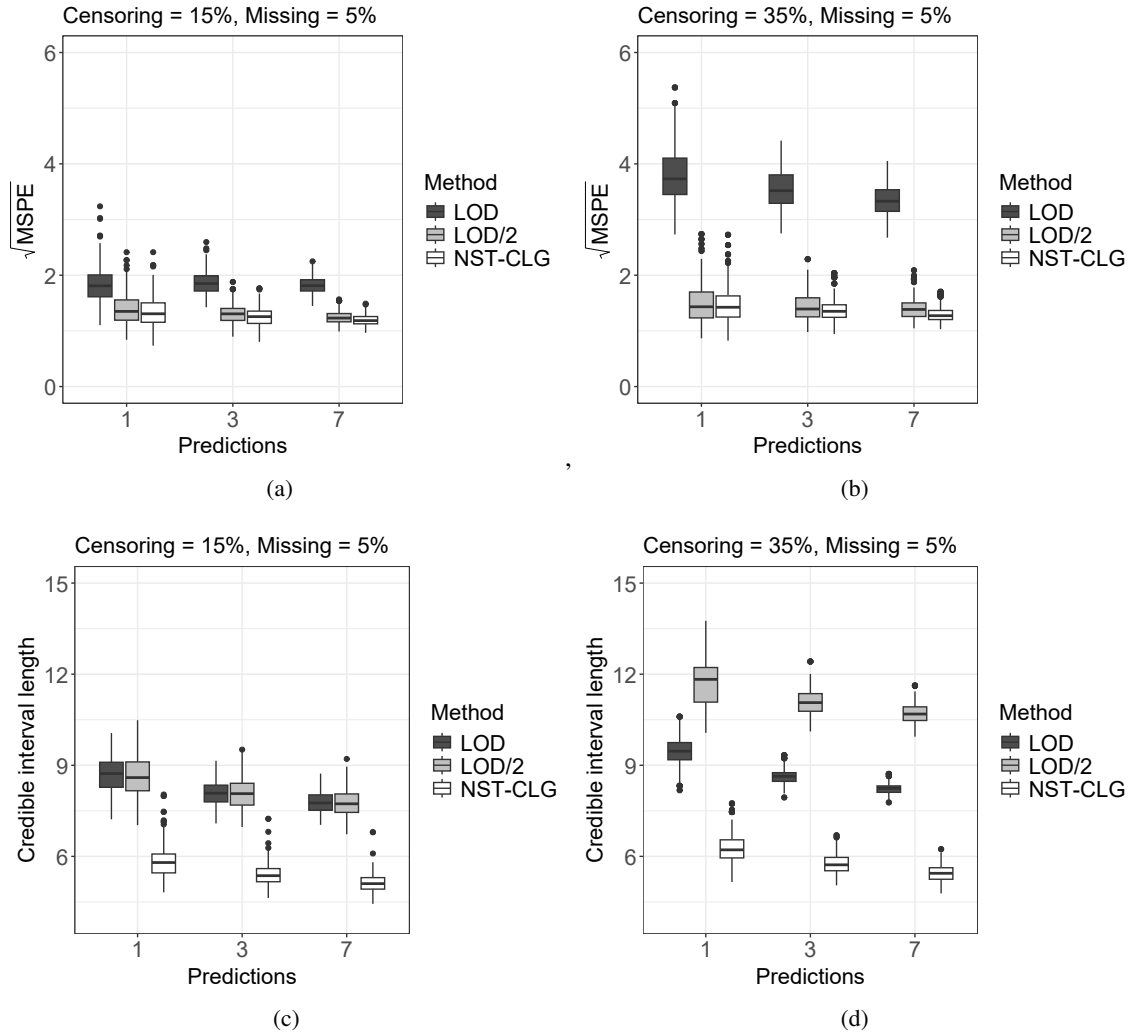


Figure 4: Simulation study II. $\sqrt{\text{MSPE}}$ and credible interval length considering a censoring level of 15% and a missing level of 5%, for one, three and seven-step-ahead predictions for $N = 500$.

6 Beijing CO concentrations spatiotemporal modeling

In this section, we apply our spatiotemporal model proposals to the CO concentrations obtained from the Beijing multi-station air quality dataset described in Section 2. Figure S.5.17 of the Supplementary Material illustrates the neighborhood relationships among monitoring stations. Preliminary analyses suggested that temperature (TEMP, °C),

Table 3: Simulation study II. Average coverage probabilities of credible intervals as a function of the number of predicted observations, with $N = 500$.

Censoring/missignness	Method	Predicted time observations		
		One	Three	Seven
15%/5%	NST-CLG	0.966	0.963	0.966
	LOD	0.983	0.999	0.999
	LOD/2	0.996	1.000	1.000
35%/5%	NST-CLG	0.956	0.963	0.963
	LOD	0.886	0.896	0.916
	LOD/2	1.000	1.000	1.000

wind speed (WSP, m/s), and atmospheric pressure (PRES, Pa) are suitable covariates for predicting CO concentrations. All predictors were centered at zero to facilitate the interpretation of the parameters in the mean structure. We also consider a log-transformation of CO, denoted $\log(\text{CO})$, to induce symmetry in the response variable.

To gain insights into the temporal and spatial correlations, we imputed missing data using the mean value per region. We computed the autocorrelation (ACF) and partial autocorrelation (PACF) for each of the twelve sites and Moran’s I at each time point (see Figures S.5.13, S.5.14 and S.5.15 in the Supplementary Material). Moran’s I series indicates a statistically significant positive spatial autocorrelation at several time points. Likewise, the ACF and PACF panels reveal temporal dependence across sites; the gradual ACF decay coupled with a dominant lag-1 spike in the PACF is consistent with the AR(1) specification for the temporal component.

After the descriptive analysis, model (1) was fitted considering the mean structure as,

$$\mu(s_i, t_q) = \beta_0 + \beta_1 \text{TEMP}^*(s_i, t_q) + \beta_2 \text{WSP}^*(s_i, t_q) + \beta_3 \text{PRES}^*(s_i, t_q),$$

where TEMP^* , WSP^* , and PRES^* , are the centered variables defined in the description of Table 1. We also consider five correlation structures: DAGAR-AR(1), DAGAR-AR(2), CAR, SAR-AR(1), and SAR-AR(2). The last two models failed to converge, whereas the CAR model was successfully fitted using $\text{Cov}(\mathbf{Y}) = \mathbf{Q}^{-1}$ in Algorithm 1, where the precision matrix $\mathbf{Q} = \mathbf{Q}(\rho_s, \rho_t, \rho_{st})$ was defined in Prates et al. [14]. The models were estimated using three chains of 40,000 iterations each, with burn-in and thinning periods of 10,000 and 50, respectively. For model comparison, we employed the expected Akaike and Bayesian information criteria (EAIC and EBIC) to assess goodness of fit, and the expected log predictive density (ELPD) to evaluate predictive performance.

Table 4 presents the posterior estimates and model selection criteria for the Beijing air pollutant dataset under the DAGAR-AR(1), DAGAR-AR(2), and CAR correlation structures. The estimated regression coefficients were similar for all models, with credibility intervals indicating their significance. However, the covariance parameters show differences. The DAGAR-AR(1) model achieves the lowest DIC and EAIC values, suggesting a better overall fit and a more parsimonious structure than the DAGAR-AR(2) model, whose second-order temporal parameter is not significant. By contrast, the CAR model presented the highest ELPD value, indicating better predictive performance, although at the cost of greater model complexity. Overall, the DAGAR-AR(1) model strikes a good balance between interpretability and estimation efficiency. The estimated temporal parameter $\gamma_1 = 0.529$ captures the exponential decay pattern and pronounced peak observed in the empirical ACF and PACF, confirming the adequacy of the AR(1) temporal structure. Together, $\gamma_1 = 0.529$ and $\rho = 0.679$ suggest a moderate temporal and spatial dependence between observations separated by 12 hours and among neighboring regions. The coefficient $\rho\gamma_1$, on the other hand, indicates a moderate spatiotemporal association between neighbors and their past. By contrast, the CAR structure provides the best out-of-sample predictive performance. This improvement is illustrated in Figure 5 and Figure S.5.16 of the Supplementary Material. An enhanced prediction accuracy can be seen when using the CAR correlation.

Regarding convergence and diagnostics, the DAGAR AR(1) model showed stable behavior with well-mixed MCMC chains, as illustrated in Figures S.5.19 and S.5.20 of the Supplementary Material. The Gelman and Rubin statistics in Table S.5.13 of the Supplementary Material further confirm this result, indicating that the posterior estimates are reliable and that the model assumptions are met adequately.

Table 4: Beijing air pollutant data. Estimated parameters and model selection criteria for the Beijing air pollutants dataset under different correlation structures.

	DAGAR-AR(1)	DAGAR-AR(2)	CAR
β_0	7.05 (6.957,7.124)	7.047 (6.965,7.118)	7.072 (6.787,7.367)
β_1	-0,037 (-0.047,-0.028)	-0.038 (-0.047,-0.027)	-0.039 (-0.047,-0.031)
β_2	-0.226 (-0.259,-0.191)	-0.229 (-0.260,-0.197)	-0.221 (-0.249,-0.191)
β_3	-5.588 (-6.728,-4.743)	-5.742 (-6.602,-4.675)	-5.754 (-6.575,-4.866)
σ^2	0.524 (0.484,0.560)	0,522 (0.482,0.562)	4.054 (3.812,4.334)
$\rho (\rho_s)$	0.679 (0.617,0.734)	0.660 (0.592,0.735)	0.995 (0.982,0.999)
$\gamma_1(\rho_t)$	0.529 (0.446,0.604)	0.446 (0.311,0.581)	0.986 (0.958,0.996)
γ_2	—	0.091 (-0.005,0.217)	—
$\rho\gamma_1 (\rho_{st})$	0.357 (0.288,0.430)	0.294 (0.197,0.402)	0.996 (0.989,0.999)
$\rho\gamma_2$	—	0.060 (-0.003,0.140)	—
τ^2	0.149 (0.119,0.180)	0.139 (0.105,0.176)	—
DIC	4074.276	4073.508	4296.148
EAIC	4082.164	4078.842	4306.731
EBIC	4162.027	4168.689	4381.992
ELPD	-97.779	-96.897	-82.502

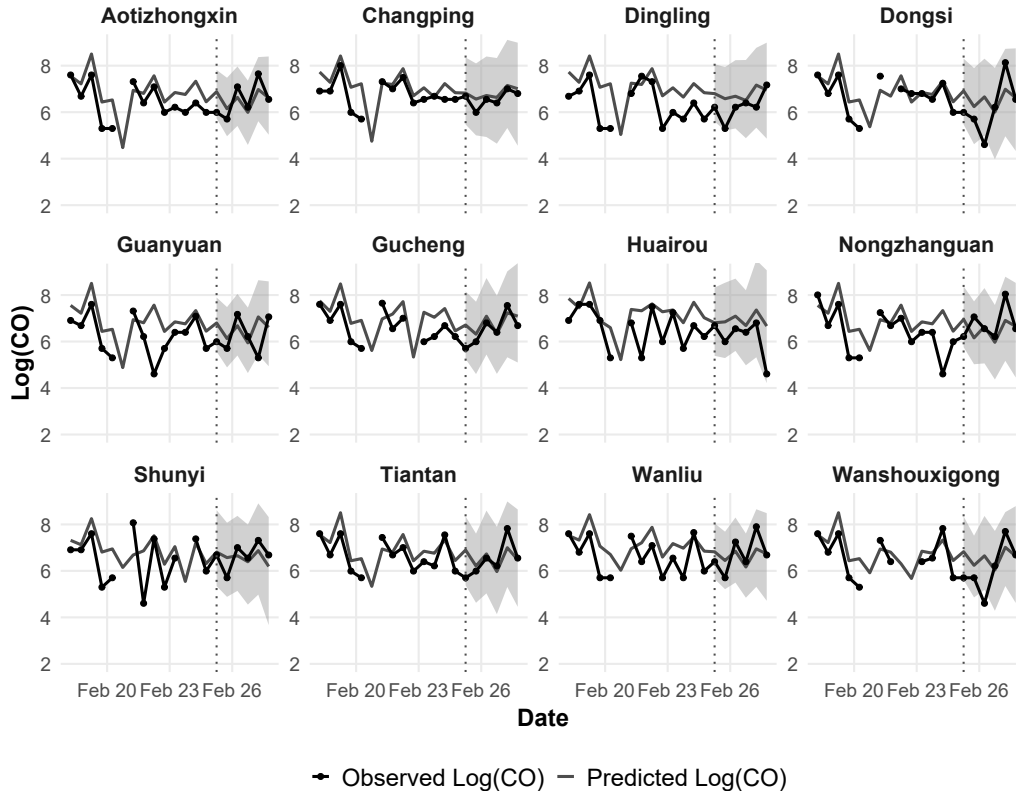


Figure 5: Beijing air pollutant data. Observed and predicted log(CO) concentrations for the CAR model across twelve monitoring stations. The shaded areas represent 95% predictive intervals.

7 Discussion

In this paper, we introduced a new methodology for analyzing spatiotemporal areal data with censored and missing responses. We propose a novel spatiotemporal random effect that jointly captures temporal autoregressive and spatial DAGAR dependencies, leading to an interpretable model structure in which the parameters can be directly understood as temporal, spatial, and spatiotemporal associations. Although our framework was developed under the multivariate normal assumption, the proposed random effect can readily be extended to non-Gaussian settings, such as count data.

Simulation studies demonstrated that our approach outperforms common ad hoc strategies for handling censored or missing data, such as replacing censored observations with LOD or LOD/2 and imputing missing values with the sample mean. Moreover, the proposed method achieved superior predictive accuracy for new observations compared to standard techniques that rely on partial information.

In the application of the log(CO) concentrations, the proposed model achieved a better fit according to the DIC, EAIC, and EBIC criteria, indicating improved interpretability and estimation efficiency. Conversely, the CAR model yielded a slightly better out-of-sample predictive performance, a trade-off that is not uncommon, as the choice between models often depends on whether the primary goal is explanation or prediction [see 11, 17].

Future research directions include extending the model to handle multiple variables, each with its own spatiotemporal correlation structure (MDAGAR), and developing analogous methods for non-Gaussian data that preserve the proposed spatiotemporal dependence. We are also interested in exploring non-separable spatiotemporal structures defined over graphs, which will be the primary focus of our forthcoming paper.

8 Acknowledgments

Jose A. Ordoñez acknowledges the financial support from the Agencia Nacional de Investigación y Desarrollo ANID, FONDECYT Postdoctorado 3240170. The work of Luis M. Castro was partially supported by the Agencia Nacional de Investigación y Desarrollo ANID, FONDECYT Regular 117029.

References

- [1] Anderson, J., Thundiyil, J., and Stolbach, A. (2011). “Clearing the air: a review of the effects of particulate matter air pollution on human health.” *Journal of Medical Toxicology*, 2(8): 166–175. 1
- [2] Banerjee, S. (2021). “Modeling massive spatial datasets using a conjugate Bayesian linear regression framework.” *Spatial Statistics*, 41: 100498.
URL <https://arxiv.org/abs/2109.04447> 10
- [3] Banerjee, S., Gelfand, A. E., and Carlin, B. P. (2025). *Hierarchical modeling and analysis for spatial data*. Boca Raton: Chapman and Hall/CRC, 3 edition.
URL <https://doi.org/10.1201/9781003401728> 5, 8
- [4] Barndorff-Nielsen, O. and Schou, G. (1973). “On the parametrization of autoregressive models by partial autocorrelations.” *Journal of Multivariate Analysis*, 3(4): 408–419. 6
- [5] Berger, O., J., De Oliveira, V., and Sansó, B. (2001). “Objective Bayesian Analysis of Spatially Correlated Data.” *Journal of the American Statistical Association*, 96(456): 1361–1374. 8
- [6] Besag, J. (1974). “Spatial interaction and statistical analysis of lattice systems.” *Journal of the Royal Statistical Society, Series B*, 36: 192–225. 2
- [7] Chen, K., Breitner, S., Wolf, K., Stafoggia, M., Sera, F., Vicedo-Cabrera, A. M., Guo, Y., Tong, S., Lavigne, E., Matus, P., Valdés, N., Kan, H., Jaakkola, J. J. K., Rytö, N. R. I., Huber, V., Scortichini, M., Hashizume, M., Honda, Y., Nunes, B., Madureira, J., Holobacă, I. H., Fratianne, S., Kim, H., Lee, W., Tobias, A., Íñiguez, C., Forsberg, B., Åström, C., Ragettli, M. S., Guo, Y.-L. L., Chen, B.-Y., Li, S., Milojevic, A., Zanobetti, A., Schwartz, J., Bell, M. L., Gasparrini, A., and Schneider, A. (2021). “Ambient carbon monoxide and daily mortality: a global time-series study in 337 cities.” *The Lancet Planetary Health*, 5(4): e191–e199. 1
- [8] Datta, A., Banerjee, S., Hodges, J. S., and Gao, L. (2019). “Spatial disease mapping using directed acyclic graph auto-regressive (DAGAR) models.” *Bayesian Analysis*, 14(4): 1221 – 1244. 2, 8
- [9] de Luna, X. and Genton, M. G. (2005). “Predictive spatio-temporal models for spatially sparse environmental data.” *Statistica Sinica*, 15: 547–568. 2
- [10] Deb, S. and Tsay, R. S. (2019). “Spatio-Temporal models with space-time Interaction and their applications to air pollution data.” *Statistica Sinica*, 29: 1181–1207. 2

- [11] Gelman, A., Hwang, J., and Vehtari, A. (2014). “Understanding predictive information criteria for Bayesian models.” *Statistics and Computing*, 24(6): 997–1016. [16](#)
- [12] Kim, Y., Yi, S.-M., Heo, J., Kim, H., Lee, W., Kim, H., Hopke, P. K., Lee, Y. S., Shin, H.-J., Park, J., Yoo, M., Jeon, K., and Park, J. (2024). “Is replacing missing values of PM2.5 constituents with estimates using machine learning better for source apportionment than exclusion or median replacement?” *Environmental Pollution*, 354: 124165. [5](#)
- [13] McMahon, K. and Launico, M. V. (2025). “Carbon monoxide toxicity.” In *StatPearls*. Treasure Island, FL: StatPearls Publishing. [1](#)
- [14] Prates, M. O., Azevedo, D. R. M., MacNab, Y. C., and Willig, M. R. (2022). “Non-separable spatio-temporal models via transformed multivariate Gaussian Markov random fields.” *Journal of the Royal Statistical Society: Series C (Applied Statistics)*, 71(5). [14](#)
- [15] Raub, J. (1999). “Health effects of exposure to ambient carbon monoxide.” *Chemosphere: Global Change Science*, (1): 331–351. [1](#)
- [16] Schelin, L. and de Luna, S. S. (2014). “Spatial prediction in the presence of left-censoring.” *Computational Statistics & Data Analysis*, 74: 125–141. [10](#)
- [17] Shmueli, G. (2010). “To explain or to predict?” *Statistical Science*, 25(3): 289–310. [16](#)
- [18] Valeriano, K. A. L., Lachos, V. H., Prates, M. O., and Matos, L. A. (2021). “Likelihood-based inference for spatiotemporal data with censored and missing responses.” *Environmetrics*, 32(3): e2663. [2](#)
- [19] Wall, M. M. (2004). “A close look at the spatial structure implied by the CAR and SAR models.” *Journal of Statistical Planning and Inference*, 121(2): 311–324. [8](#)
- [20] Wang, W. and Sun, Y. (2019). “Penalized local polynomial regression for spatial data.” *Biometrics*, 75(4): 1179–1190. [2](#)
- [21] Wardana, I. N. K., Gardner, J. W., and Fahmy, S. A. (2022). “Estimation of missing air pollutant data using a spatiotemporal convolutional autoencoder.” *Neural Computing and Applications*, 34: 16129–16154. [3](#)
- [22] Whittle, P. (1954). “On stationary process in the plane.” *Biometrika*, 41: 434–449. [2](#)
- [23] Zhang, S., Guo, B., Dong, A., He, J., Xu, Z., and Chen, S. X. (2017). “Cautionary tales on air-quality improvement in Beijing.” *Proceedings of the Royal Society A: Mathematical, Physical and Engineering Sciences*, 473. [2](#)

9 Appendix

9.1 Proof of Proposition 3.1

Given the correlation matrix in equation (5) of the main manuscript, and a fixed position \mathbf{s}_i , $\boldsymbol{\omega}_{\mathbf{s}_i}$ can be written as,

$$\omega(\mathbf{s}_i, t_j) = \gamma_1 \omega(\mathbf{s}_i, t_{j-1}) + \gamma_2 \omega(\mathbf{s}_i, t_{j-2}) + \dots + \gamma_p \omega(\mathbf{s}_i, t_{j-p}) + \epsilon(\mathbf{s}_i, t_j),$$

with $\epsilon(\mathbf{s}_i, t_j) \sim N(0, \sigma^2)$, $t > p$, $k = 1, \dots, p$. Denote the backward shift matrices as $\mathbf{J}^1, \dots, \mathbf{J}^p$, with $[\mathbf{J}^k]_{(t, t-k)} = 1$, for $t > k$ and 0 elsewhere. Then, we can write the process in its vectorial form,

$$\boldsymbol{\omega}_{\mathbf{s}_i} = \gamma_1 \mathbf{J}^1 \boldsymbol{\omega}_{\mathbf{s}_i} + \dots + \gamma_p \mathbf{J}^p \boldsymbol{\omega}_{\mathbf{s}_i} + \boldsymbol{\epsilon}_{\mathbf{s}_i},$$

with $\boldsymbol{\epsilon}_{\mathbf{s}_i} = (\epsilon(\mathbf{s}_i, t_1), \dots, \epsilon(\mathbf{s}_i, t_T)) \sim N(0, \mathbf{D})$ and $\mathbf{D} = \text{diag}(\sigma^2)$. Therefore,

$$(\mathbf{I} - \gamma_1 \mathbf{J}^1 - \dots - \gamma_p \mathbf{J}^p) \boldsymbol{\omega}_{\mathbf{s}_i} = \boldsymbol{\epsilon}_{\mathbf{s}_i}. \quad (17)$$

If we set $\mathbf{B}_T = \sum_{k=1}^p \gamma_k \mathbf{J}^k$, and $\mathbf{F}_T = \text{diag}(1/\sigma^2)$, then, we can deduce from (17), that $\boldsymbol{\omega}_{\mathbf{s}_i}$ can be written as a directed acyclic graph and that $\boldsymbol{\omega}_{\mathbf{s}_i} \sim N_T(\mathbf{0}, [(\mathbf{I}_T - \mathbf{B}_T)^\top \mathbf{F}_T (\mathbf{I}_T - \mathbf{B}_T)]^{-1})$. Therefore, $\boldsymbol{\omega}_{\mathbf{s}_i}$ follows a T-variate normal distribution as settled in Proposition 3.1 of the main manuscript. \square

9.2 Proof of Theorem 3.1

From Proposition 3.1 of the main manuscript, we can represent $\sigma^2\Phi = [(\mathbf{I}_T - \mathbf{B}_T)^\top \mathbf{F}_T (\mathbf{I}_T - \mathbf{B}_T)]^{-1}$. Also, given the SAR/DAGAR structure, we can represent the spatial covariance as $\Sigma = [(\mathbf{I}_n - \mathbf{B}_n)^\top \mathbf{F}_n (\mathbf{I}_n - \mathbf{B}_n)]$ with \mathbf{B}_n and \mathbf{F}_n defined for both cases in Subsection 3.1 of the main manuscript. Therefore, by the Kronecker product properties,

$$\begin{aligned} \Sigma \otimes \sigma^2\Phi &= [(\mathbf{I}_n - \mathbf{B}_n)^\top \mathbf{F}_n (\mathbf{I}_n - \mathbf{B}_n)]^{-1} \otimes [(\mathbf{I}_T - \mathbf{B}_T)^\top \mathbf{F}_T (\mathbf{I}_T - \mathbf{B}_T)]^{-1} \\ &= [(\mathbf{I}_n - \mathbf{B}_n)^{-1} \otimes (\mathbf{I}_T - \mathbf{B}_T)^{-1}] \mathbf{F}_n^{-1} \otimes \mathbf{F}_T^{-1} [(\mathbf{I}_n - \mathbf{B}_n)^{-1} \otimes (\mathbf{I}_T - \mathbf{B}_T)^{-1}]^\top \\ &= [(\mathbf{I}_n - \mathbf{B}_n) \otimes (\mathbf{I}_T - \mathbf{B}_T)]^{-1} (\mathbf{F}_n \otimes \mathbf{F}_T)^{-1} \{[(\mathbf{I}_n - \mathbf{B}_n) \otimes (\mathbf{I}_T - \mathbf{B}_T)]^{-1}\}^\top \\ &= \{[(\mathbf{I}_n - \mathbf{B}_n) \otimes (\mathbf{I}_T - \mathbf{B}_T)]^\top (\mathbf{F}_n \otimes \mathbf{F}_T) [(\mathbf{I}_n - \mathbf{B}_n) \otimes (\mathbf{I}_T - \mathbf{B}_T)]\}^{-1} \end{aligned}$$

Now,

$$\begin{aligned} (\mathbf{I}_n - \mathbf{B}_n) \otimes (\mathbf{I}_T - \mathbf{B}_T) &= (\mathbf{I}_n \otimes \mathbf{I}_T - \mathbf{I}_n \otimes \mathbf{B}_T - \mathbf{B}_n \otimes \mathbf{I}_T + \mathbf{B}_n \otimes \mathbf{B}_T) \\ &= \mathbf{I}_{nT} - \mathbf{B}_{nT}, \end{aligned}$$

where \mathbf{I}_{nT} is the identity matrix of order nT and $\mathbf{B}_{nT} = \mathbf{I}_n \otimes \mathbf{B}_T + \mathbf{B}_n \otimes \mathbf{I}_T - \mathbf{B}_n \otimes \mathbf{B}_T$. Then,

$$\Sigma \otimes \sigma^2\Phi = [(\mathbf{I}_{nT} - \mathbf{B}_{nT})^\top \mathbf{F}_{nT} (\mathbf{I}_{nT} - \mathbf{B}_{nT})]^{-1}$$

with $\mathbf{F}_{nT} = \mathbf{F}_n \otimes \mathbf{F}_T$. Then $\boldsymbol{\omega} \sim N_{n \times T}(\mathbf{0}, [(\mathbf{I}_{nT} - \mathbf{B}_{nT})^\top \mathbf{F}_{nT} (\mathbf{I}_{nT} - \mathbf{B}_{nT})]^{-1})$ and therefore, it can be expressed as a SAR/DAGAR process depending on the definition of $\mathbf{B}_n, \mathbf{F}_n$. Note that we can express equations (10) and (11) in its matrix form, i.e.,

$$\boldsymbol{\omega} = (\mathbf{I}_n \otimes \mathbf{B}_T)\boldsymbol{\omega} + (\mathbf{B}_n \otimes \mathbf{I}_T)\boldsymbol{\omega} - (\mathbf{B}_n \otimes \mathbf{B}_T)\boldsymbol{\omega} + \boldsymbol{\epsilon} \quad \square$$

9.3 Proof of Proposition 4.1

Let $\boldsymbol{\lambda} = (\rho, \psi, \phi)$ the parameters associated to the covariance structure. The posterior $\pi(\boldsymbol{\beta}, \sigma^2, \boldsymbol{\lambda} \mid \mathbf{y})$ can be rewritten as,

$$\pi(\boldsymbol{\beta}, \sigma^2, \boldsymbol{\lambda} \mid \mathbf{y}) \propto \pi(\boldsymbol{\beta}, \sigma^2 \mid \boldsymbol{\lambda}, \mathbf{y}) \pi(\boldsymbol{\lambda} \mid \mathbf{y}).$$

Also,

$$\pi(\boldsymbol{\beta}, \sigma^2 \mid \boldsymbol{\lambda}, \mathbf{y}) \propto \pi(\boldsymbol{\beta}, \sigma^2 \mid \boldsymbol{\lambda}) \mathbf{L}(\boldsymbol{\beta}, \sigma^2, \boldsymbol{\lambda} \mid \mathbf{y}),$$

then,

$$\pi(\boldsymbol{\lambda} \mid \mathbf{y}) \propto \frac{\pi(\boldsymbol{\beta}, \sigma \mid \boldsymbol{\lambda}) \mathbf{L}(\boldsymbol{\beta}, \sigma^2, \boldsymbol{\lambda} \mid \mathbf{y})}{\pi(\boldsymbol{\beta}, \sigma^2 \mid \boldsymbol{\lambda}, \mathbf{y})} \pi(\boldsymbol{\lambda}). \quad (18)$$

For our particular case, we have,

$$\pi(\boldsymbol{\beta}, \sigma^2 | \boldsymbol{\lambda}, \mathbf{y}) \propto \frac{1}{|V_{\hat{\boldsymbol{\beta}}}|^{\frac{1}{2}}} \exp \left[-\frac{(\boldsymbol{\beta} - \hat{\boldsymbol{\beta}})^\top V_{\hat{\boldsymbol{\beta}}}^{-1} (\boldsymbol{\beta} - \hat{\boldsymbol{\beta}})}{2\sigma^2} \right] \times$$

$$(S^2)^{\frac{n-p}{2}} (\sigma^2)^{-\left(\frac{v}{2}+1\right)} \exp \left\{ -\frac{(n-p)S^2}{2\sigma^2} \right\} \quad (19)$$

$$L(\boldsymbol{\beta}, \sigma^2, \boldsymbol{\lambda} | \mathbf{y}) \propto \frac{1}{(\sigma^2)^{n/2} |\boldsymbol{\Sigma}_\psi|^{1/2}} \exp \left[-\frac{(\mathbf{y} - \mathbf{X}\boldsymbol{\beta})^\top \boldsymbol{\Sigma}_\psi^{-1} (\mathbf{y} - \mathbf{X}\boldsymbol{\beta})}{2\sigma^2} \right] \quad (20)$$

$$\pi(\boldsymbol{\beta}, \sigma^2 | \boldsymbol{\lambda}) \pi(\boldsymbol{\lambda}) \propto \frac{\pi(\boldsymbol{\lambda})}{\sigma^2}, \quad (21)$$

with S_ψ^2 , $V_{\hat{\boldsymbol{\beta}}}$ and $\hat{\boldsymbol{\beta}}$ as defined at the end of Proposition 3.1. Substituting,

$$(\mathbf{y} - \mathbf{X}\boldsymbol{\beta})^\top \boldsymbol{\Sigma}_\psi^{-1} (\mathbf{y} - \mathbf{X}\boldsymbol{\beta}) = (\boldsymbol{\beta} - \hat{\boldsymbol{\beta}})^\top V_{\hat{\boldsymbol{\beta}}}^{-1} (\boldsymbol{\beta} - \hat{\boldsymbol{\beta}}) + (\mathbf{y} - \mathbf{X}\hat{\boldsymbol{\beta}})^\top \boldsymbol{\Sigma}_\psi^{-1} (\mathbf{y} - \mathbf{X}\hat{\boldsymbol{\beta}})$$

in equation (20), and then substituting (19), (20) and (21) in equation (18), the exponential terms in (19) and (20) will vanish. After some additional algebra we get,

$$\pi(\boldsymbol{\lambda} | \mathbf{y}) \propto |\boldsymbol{\Sigma}_\psi|^{1/2} |V_{\hat{\boldsymbol{\beta}}}|^{1/2} (S^2)^{-n-p/2} \pi(\boldsymbol{\lambda}) \quad \square$$

10 Additional Simulation results

Table 5: Simulation study 1 - DAGAR model. Coverage probabilities of the mean structure parameters considering a level of censoring of 15%

N	Parameter	NST-CLG	LOD	LOD/2
81	β_0	0.953	0.013	0.983
	β_1	0.970	0.030	0.907
	β_2	0.943	0.000	0.917
256	β_0	0.937	0.000	0.880
	β_1	0.920	0.000	0.583
	β_2	0.930	0.000	0.600
625	β_0	0.937	0.000	0.663
	β_1	0.957	0.000	0.240
	β_2	0.940	0.000	0.360

Table 6: Simulation study 1 - DAGAR model. Coverage probabilities of the mean structure parameters considering a level of censoring of 35%

N	Parameter	NST-CLG	LOD	LOD/2
81	β_0	0.953	0.000	0.893
	β_1	0.933	0.003	0.973
	β_2	0.940	0.000	0.957
256	β_0	0.917	0.000	1.000
	β_1	0.910	0.000	0.990
	β_2	0.937	0.000	0.533
625	β_0	0.927	0.000	0.993
	β_1	0.920	0.000	0.477
	β_2	0.943	0.000	0.190

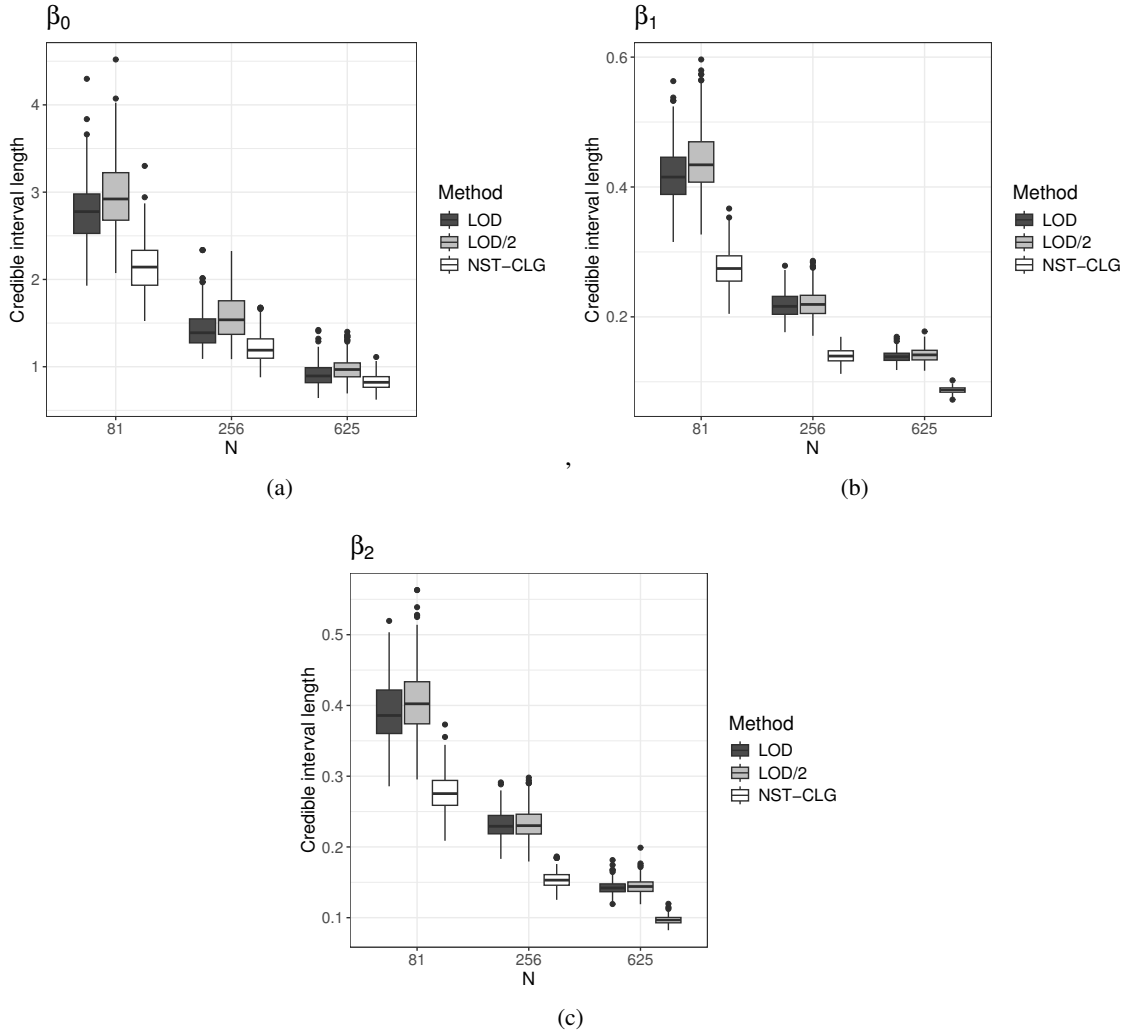


Figure 6: Simulation study 1 - DAGAR model. Credible interval lengths for the mean structure parameters considering a censoring level of 15% and missing level of 5%

Table 7: Simulation study 1 - DAGAR model. Coverage probabilities of the covariance structure parameters considering a level of censoring of 35%

N	Parameter	NST-CLG	LOD	LOD/2
81	σ^2	1.000	0.010	0.000
	ρ	0.993	0.980	0.980
	τ^2	0.957	0.990	0.220
	ϕ	0.997	0.860	1.000
256	σ^2	1.000	0.000	0.000
	ρ	0.993	0.870	0.870
	τ^2	0.937	0.997	0.133
	ϕ	0.943	0.4530	0.893
625	σ^2	0.997	0.000	0.000
	ρ	0.963	0.653	0.653
	τ^2	0.920	0.983	0.107
	ϕ	0.950	0.463	0.853

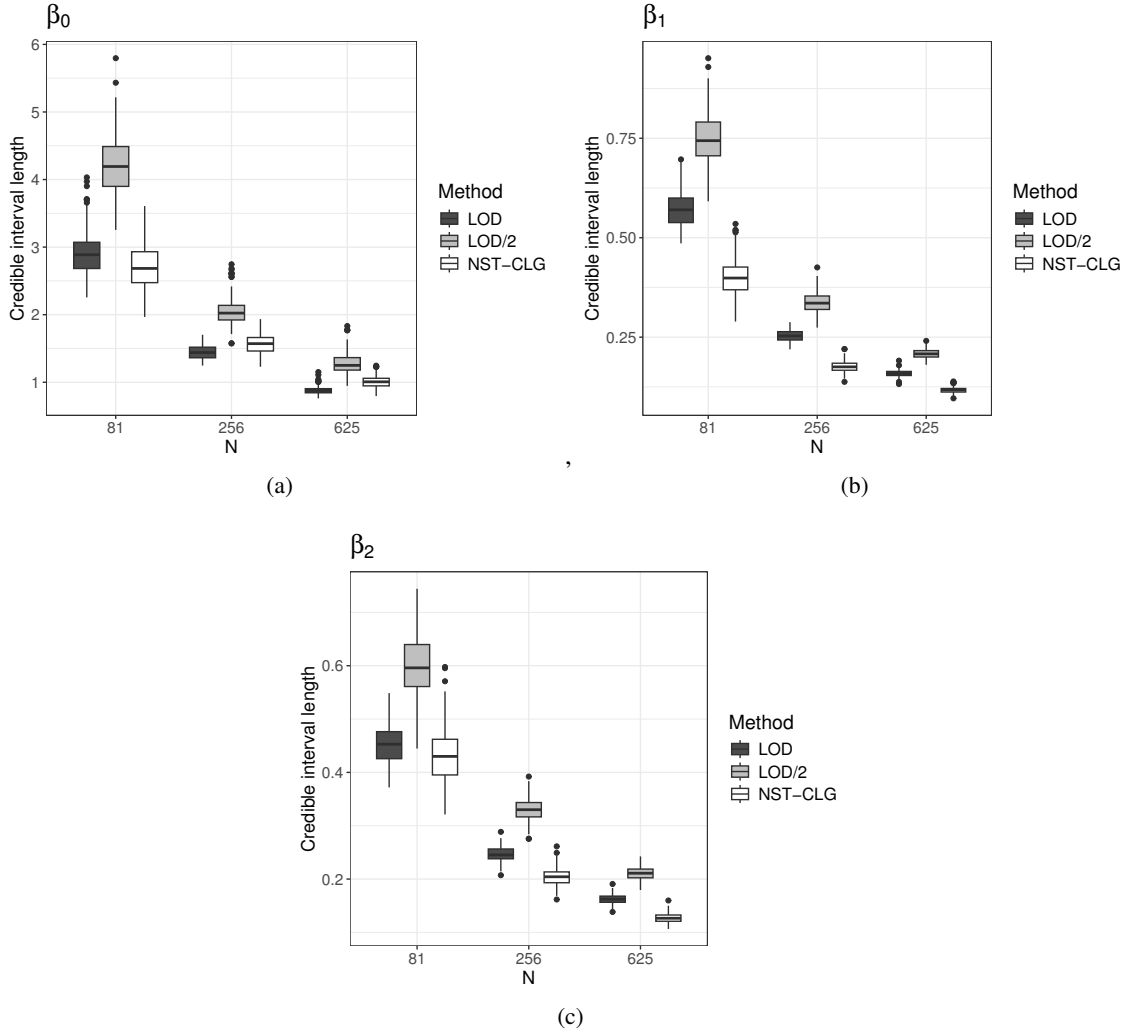


Figure 7: Simulation study 1 - DAGAR model. Credible interval lengths for the mean structure parameters with censoring level $c = 0.35$ and missing level $miss = 0.05$.

Table 8: Simulation study 1 - SAR model. Coverage probabilities of the mean structure parameters considering a level of censoring of 15%

N	Parameter	NST-CLG	LOD	LOD/2
81	β_0	0.903	0.133	0.903
	β_1	0.920	0.020	0.740
	β_2	0.950	0.000	0.847
256	β_0	0.923	0.040	0.720
	β_1	0.933	0.000	0.520
	β_2	0.960	0.000	0.380
625	β_0	0.923	0.000	0.800
	β_1	0.930	0.000	0.530
	β_2	0.933	0.000	0.280

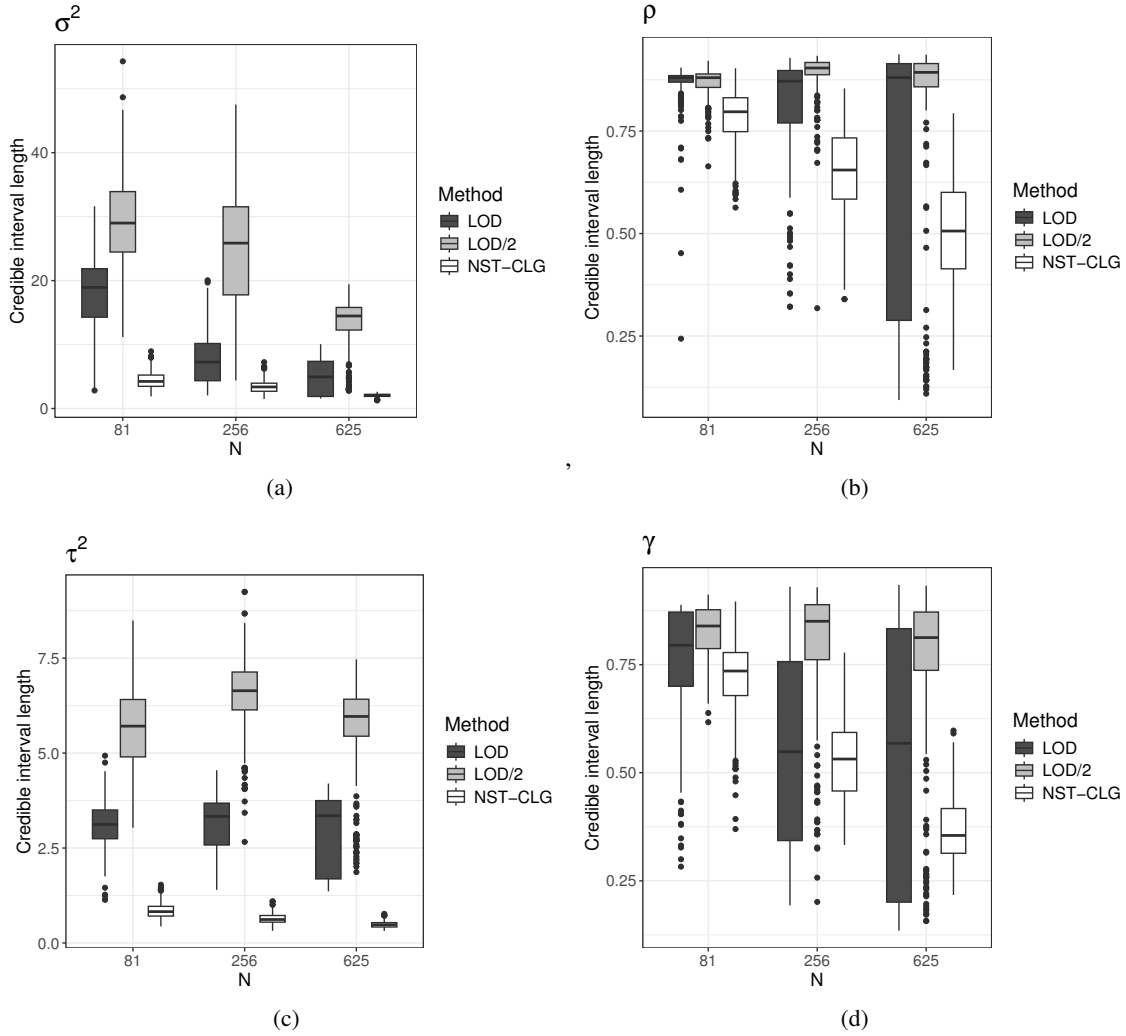


Figure 8: Simulation study 1 - DAGAR model. Credible interval lengths for the covariance structure parameters with censoring level $c = 0.35$ and missing level $miss = 0.05$.

Table 9: Simulation study 1 - SAR model. Coverage probabilities of the mean structure parameters considering a level of censoring of 35%

N	Parameter	NST-CLG	LOD	LOD/2
81	β_0	0.937	0.007	0.770
	β_1	0.953	0.000	0.820
	β_2	0.960	0.000	0.927
256	β_0	0.907	0.000	0.497
	β_1	0.957	0.000	0.043
	β_2	0.943	0.000	0.463
625	β_0	0.950	0.000	0.463
	β_1	0.920	0.000	0.040
	β_2	0.933	0.000	0.117

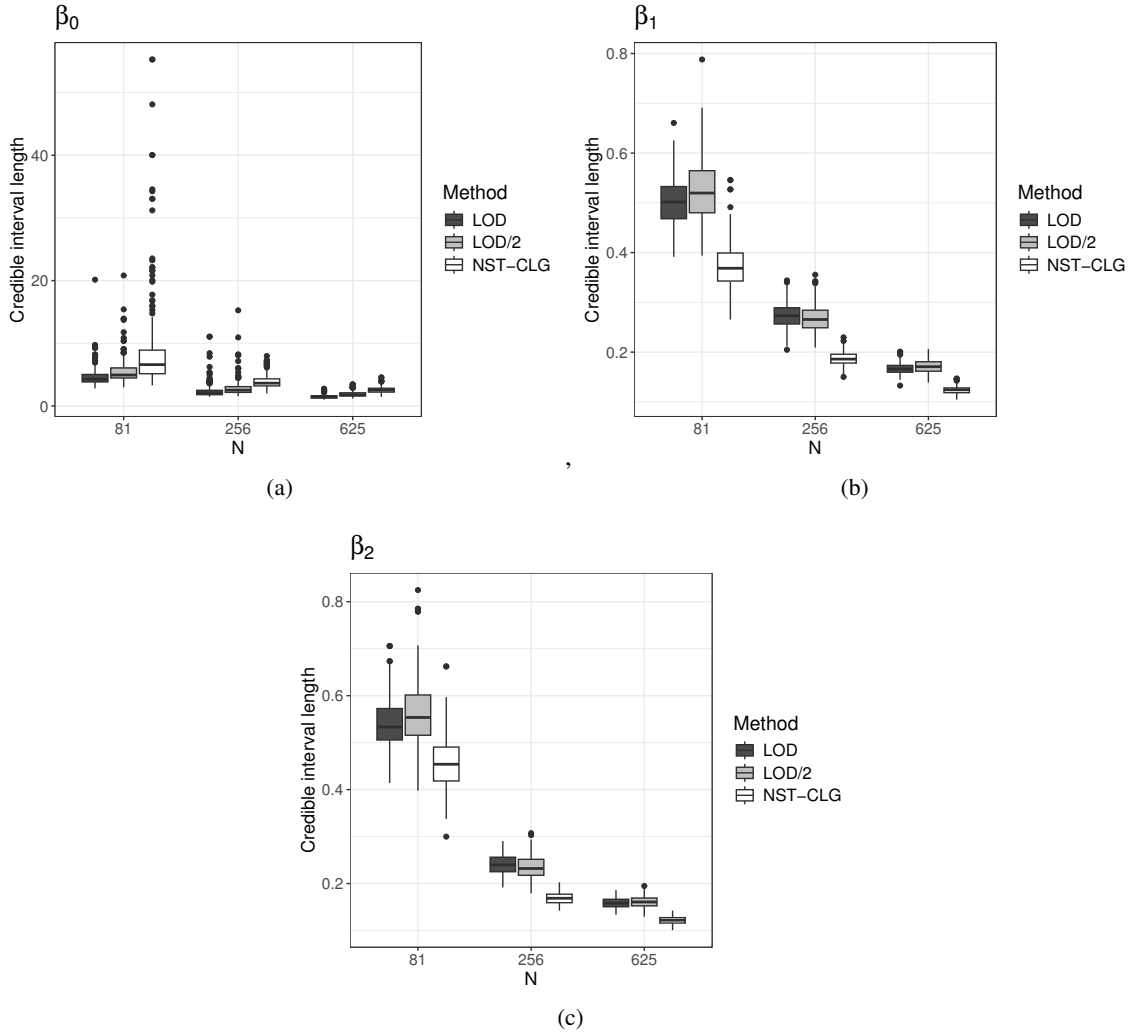


Figure 9: Simulation study 1 - SAR model. Credible interval lengths for the mean structure parameters considering a censoring level of 15% and missing level of 5%

Table 10: Simulation study 1 - SAR model. Coverage probabilities of the covariance structure parameters considering a level of censoring of 15%

N	Parameter	NST-CLG	LOD	LOD/2
81	σ^2	0.937	0.000	0.000
	ρ	0.930	0.253	0.253
	τ^2	0.990	0.897	0.740
	ϕ	0.957	0.870	0.883
256	σ^2	0.990	0.000	0.000
	ρ	0.960	0.050	0.050
	τ^2	0.990	0.673	0.590
	ϕ	0.977	0.563	0.740
625	σ^2	0.960	0.000	0.000
	ρ	0.980	0.027	0.027
	τ^2	0.973	0.187	0.027
	ϕ	0.977	0.303	0.617

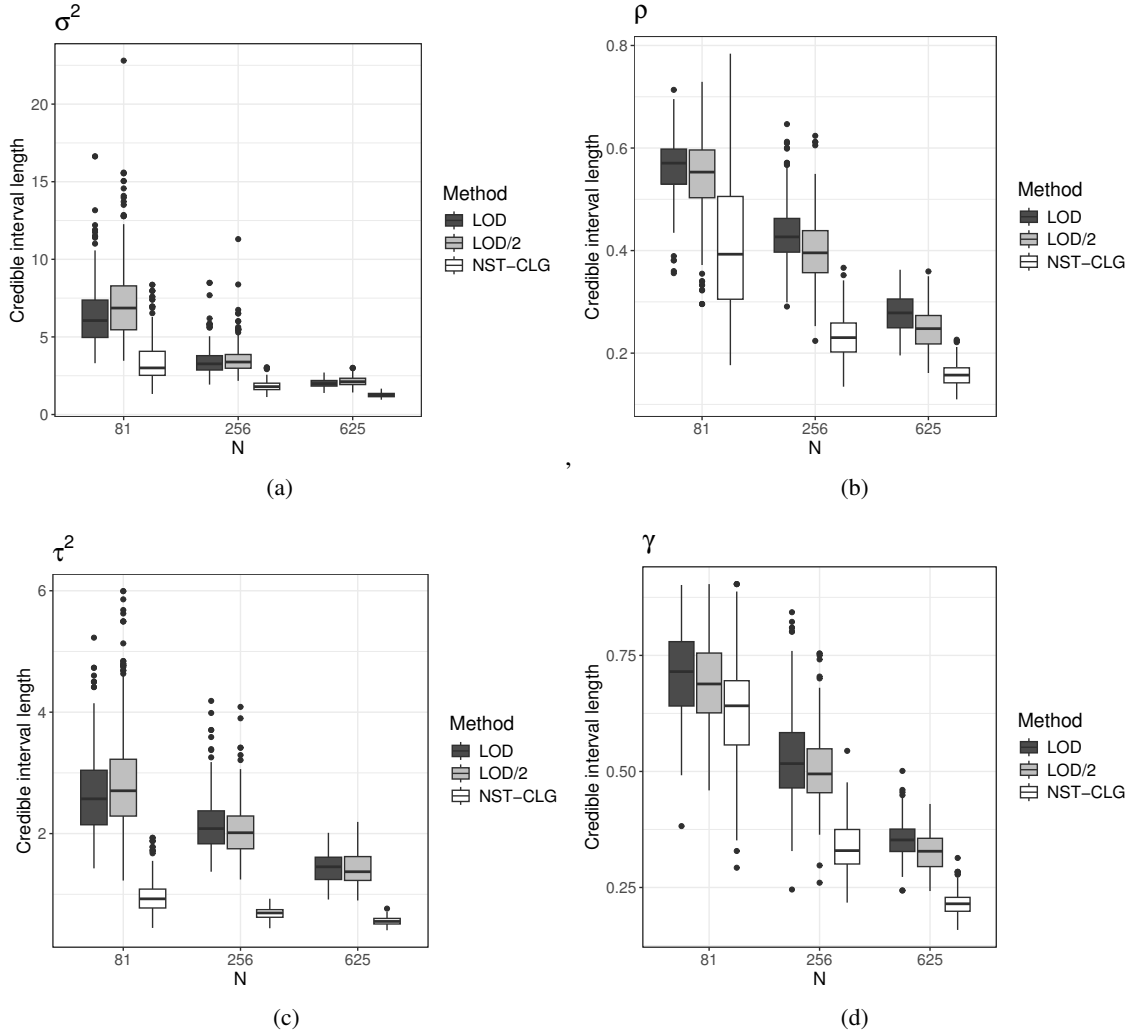


Figure 10: Simulation study 1 - SAR model. Credible interval lengths for the covariance structure parameters considering a censoring level of 15% and missing level of 5%

Table 11: Simulation study 1 - SAR model. Coverage probabilities of the covariance structure parameters considering a level of censoring of 35%

N	Parameter	NST-CLG	LOD	LOD/2
81	σ^2	0.923	0.003	0.000
	ρ	0.933	0.067	0.067
	τ^2	0.993	0.917	0.093
	ϕ	0.970	0.437	0.767
256	σ^2	0.980	0.000	0.000
	ρ	0.953	0.830	0.013
	τ^2	1.000	0.903	0.090
	ϕ	0.973	0.213	0.330
625	σ^2	0.983	0.000	0.000
	ρ	0.970	0.000	0.000
	τ^2	0.993	0.610	0.000
	ϕ	0.977	0.027	0.200

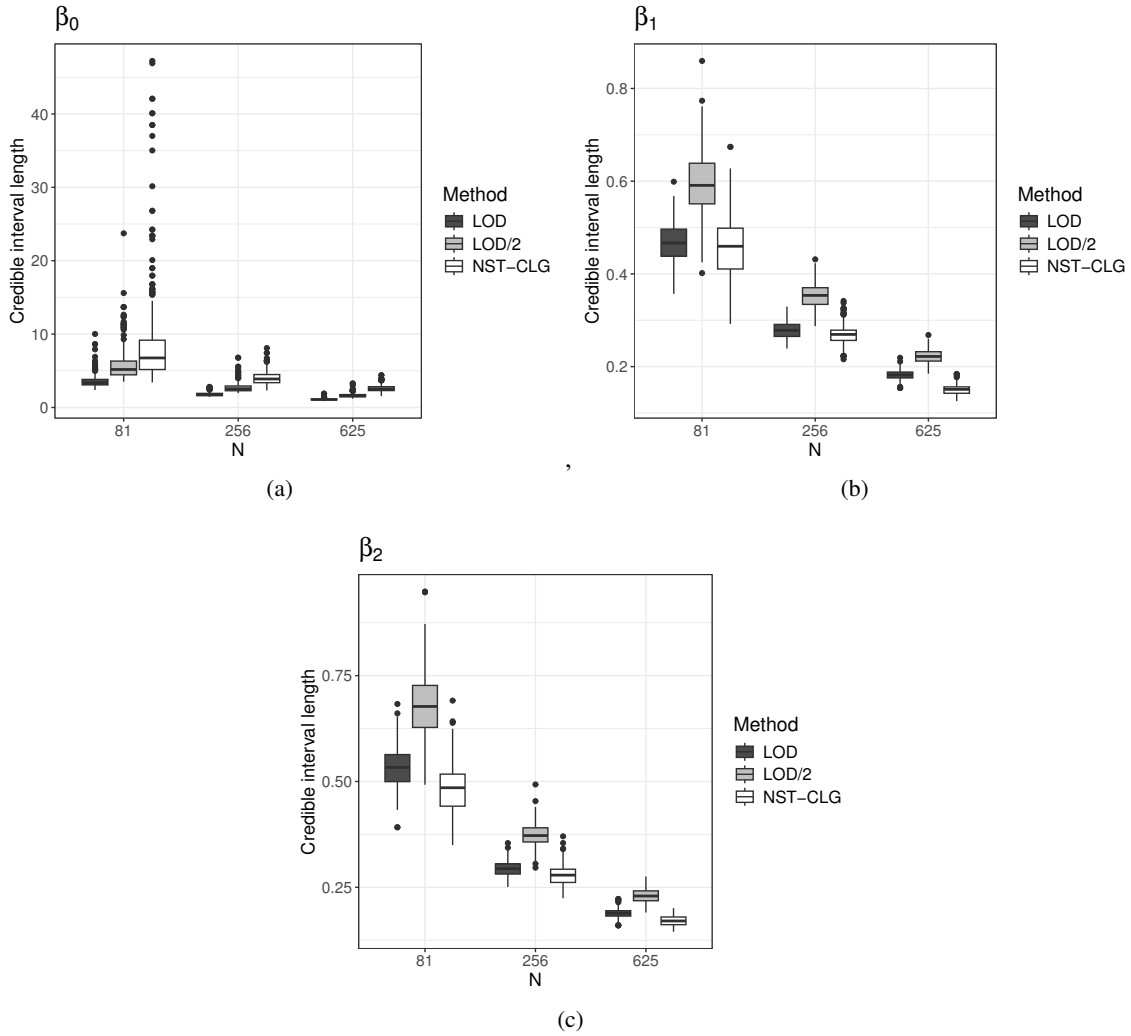


Figure 11: Simulation study 1 - SAR model. Credible interval lengths for the mean structure parameters with censoring level $c = 0.35$ and missing level $miss = 0.05$.

Table 12: Simulation study 2 - DAGAR model. Average coverage probabilities of credible intervals varying the number of predicted observations, considering $N = 250$.

Censoring/missignness	Method	Predicted time observations		
		One	Three	Seven
20%	MTN	0.966	0.966	0.970
	LOD	0.993	0.990	0.986
	LOD/2	0.996	1.000	1.000
40%	MTN	0.983	0.980	0.980
	LOD	0.956	0.963	0.960
	LOD/2	1.000	1.000	1.000

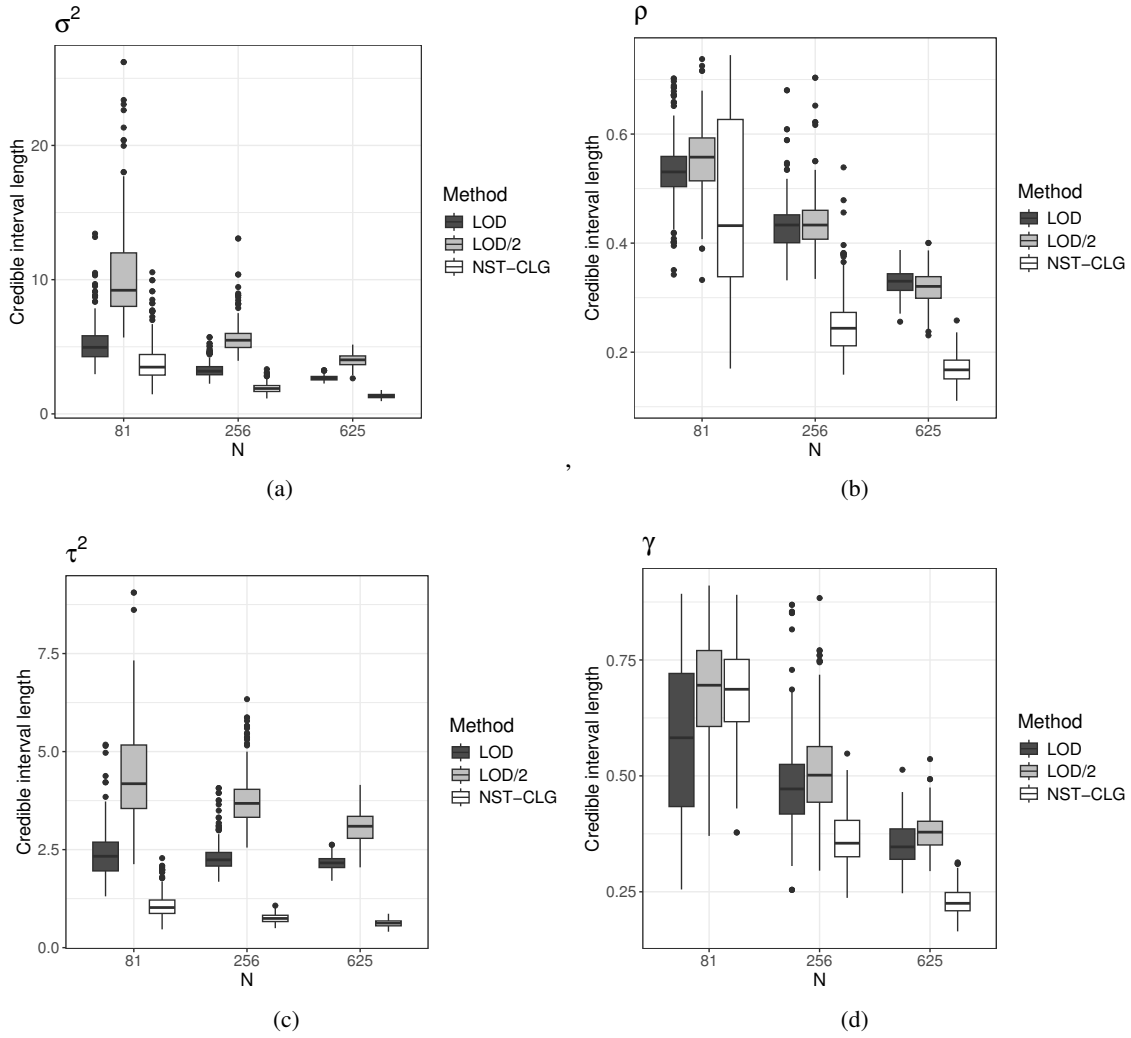


Figure 12: Simulation study 1 - SAR model. Credible interval lengths for the covariance structure parameters with censoring level $c = 0.35$ and missing level $miss = 0.05$.

Table 13: Simulation study 2 - DAGAR model. Average coverage probabilities of credible intervals varying the number of predicted observations, considering $N = 750$.

Censoring/missignness	Method	Predicted time observations		
		One	Three	Seven
20%	MTN	0.953	0.960	0.966
	LOD	0.990	0.990	0.990
	LOD/2	0.996	1.000	1.000
40%	MTN	0.966	0.973	0.973
	LOD	0.936	0.923	0.923
	LOD/2	1.000	1.000	1.000

Table 14: Simulation study 2 - SAR model. Average coverage probabilities of credible intervals varying the number of predicted observations, considering $N = 250$.

Censoring/missignness	Method	Predicted time observations		
		One	Three	Seven
20%	MTN	0.940	0.940	0.946
	LOD	0.926	0.920	0.923
	LOD/2	0.963	0.966	0.970
40%	MTN	0.933	0.936	0.936
	LOD	0.860	0.873	0.870
	LOD/2	0.976	0.980	0.980

Table 15: Simulation study 2 - SAR model. Average coverage probabilities of credible intervals varying the number of predicted observations, considering $N = 500$.

Censoring/missignness	Method	Predicted time observations		
		One	Three	Seven
20%	MTN	0.940	0.940	0.943
	LOD	0.930	0.930	0.940
	LOD/2	0.956	0.960	0.963
40%	MTN	0.933	0.933	0.940
	LOD	0.830	0.826	0.830
	LOD/2	0.983	0.986	0.986

Table 16: Simulation study 2 - SAR model. Average coverage probabilities of credible intervals varying the number of predicted observations, considering $N = 750$.

Censoring/missignness	Method	Predicted time observations		
		One	Three	Seven
20%	MTN	0.950	0.943	0.940
	LOD	0.936	0.930	0.930
	LOD/2	0.960	0.963	0.966
40%	MTN	0.940	0.943	0.943
	LOD	0.886	0.850	0.846
	LOD/2	0.986	0.986	0.986

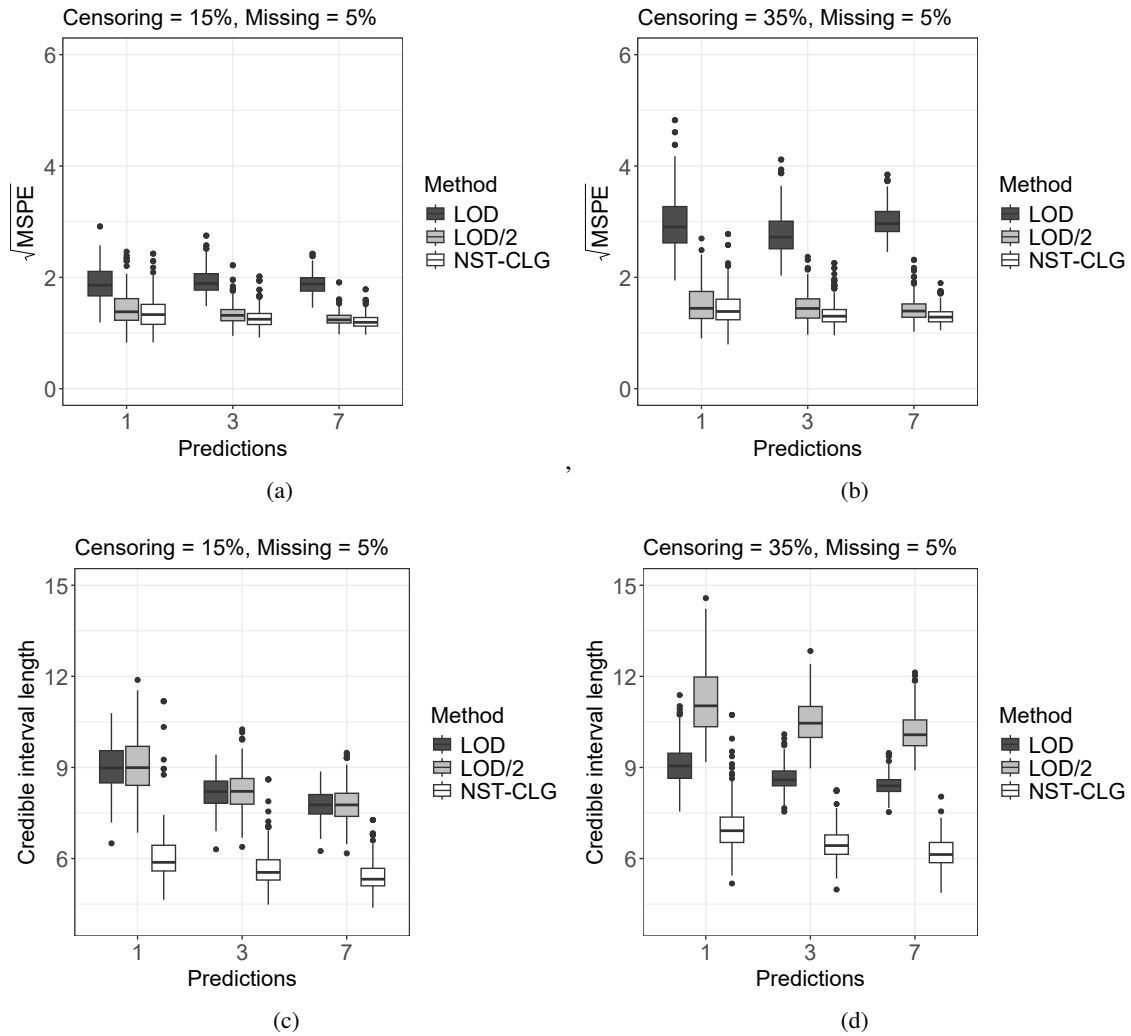


Figure 13: Simulation study 2 - DAGAR model. Comparison of our proposal (NST-CLG) with methods that impute the censored observations by using the limit of detection. For this scenario, we consider $N = 250$.

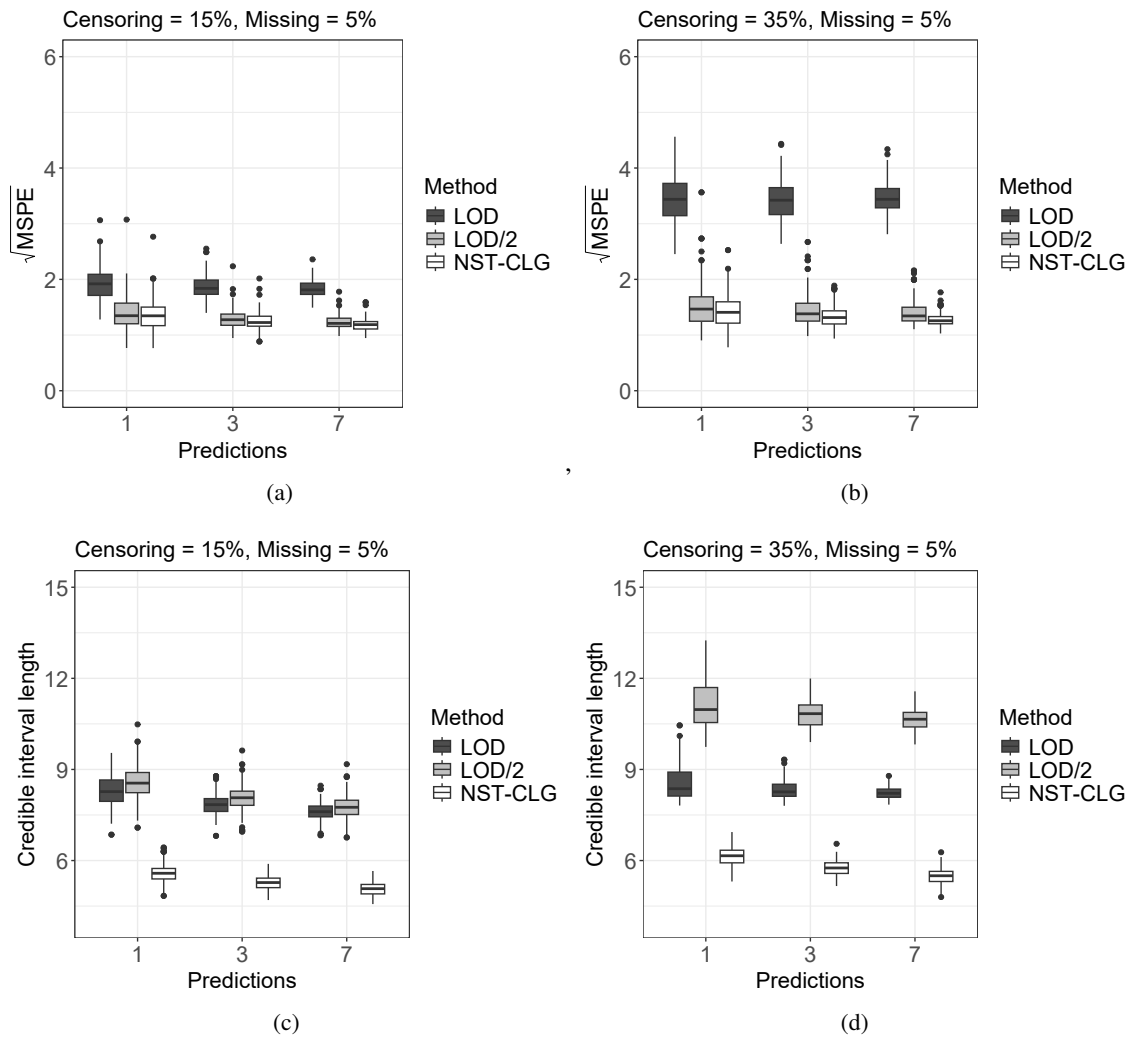


Figure 14: Simulation study 2 - DAGAR model. Comparison of our proposal (NST-CLG) with methods that impute the censored observations by using the limit of detection. For this scenario, we consider $N = 750$.

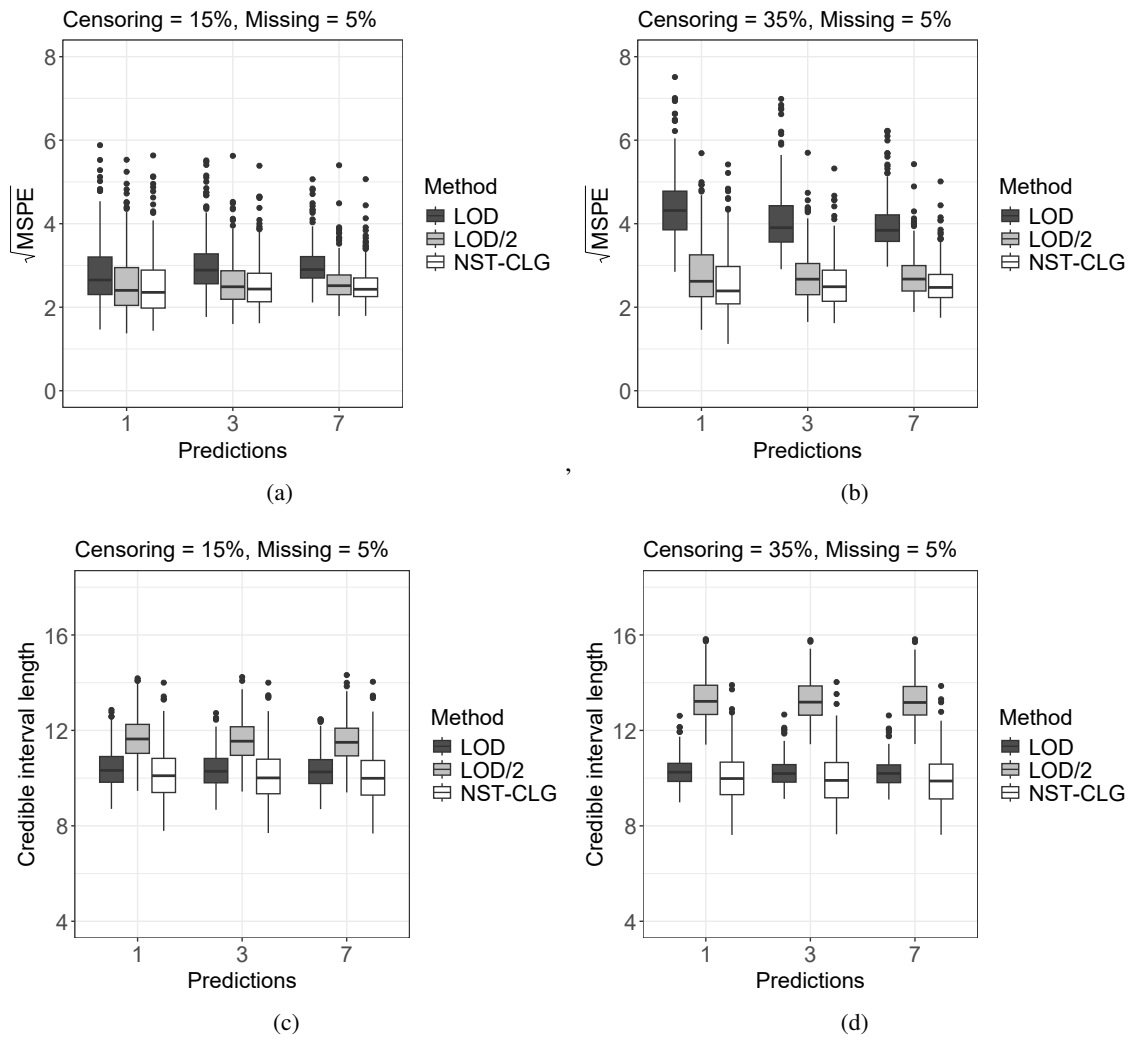


Figure 15: Simulation study 2 - SAR model. Comparison of our proposal (NST-CLG) with methods that impute the censored observations by using the limit of detection. For this scenario, we consider $N = 250$.

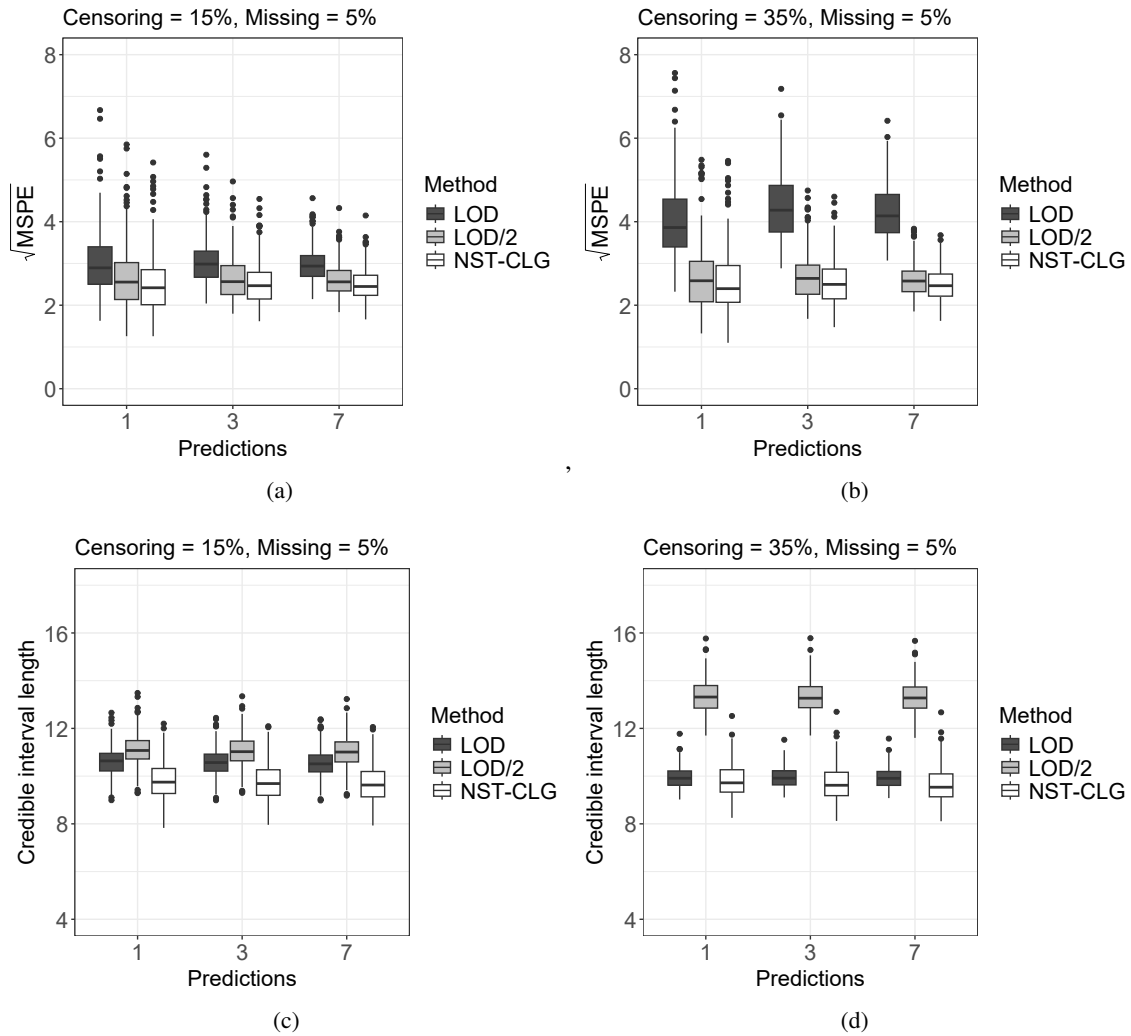


Figure 16: Simulation study 2 - SAR model. Comparison of our proposal (NST-CLG) with methods that impute the censored observations by using the limit of detection. For this scenario, we consider $N = 500$.

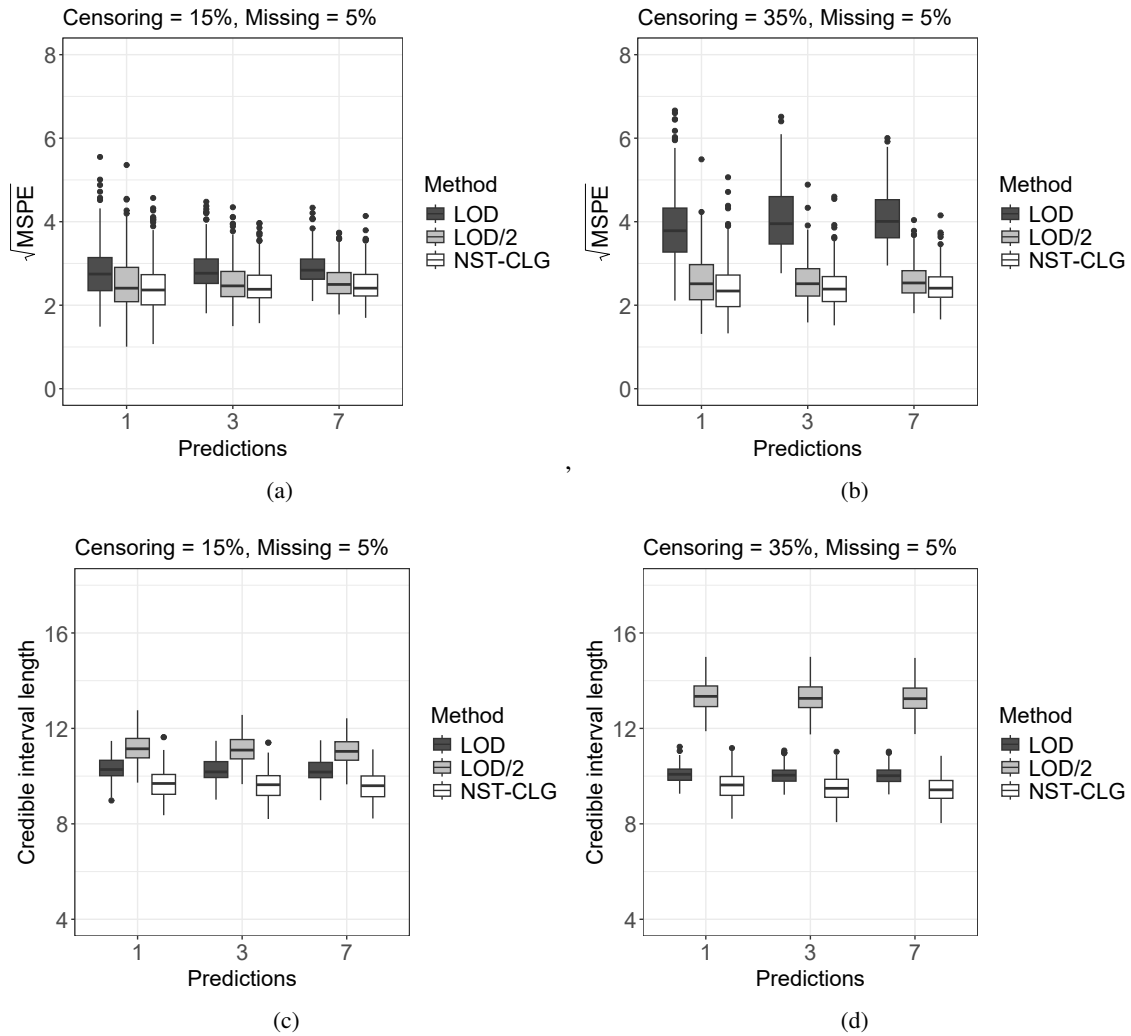


Figure 17: Simulation study 2 - SAR model. Comparison of our proposal (NST-CLG) with methods that impute the censored observations by using the limit of detection. For this scenario, we consider $N = 750$.

11 Beijing data: Additional results

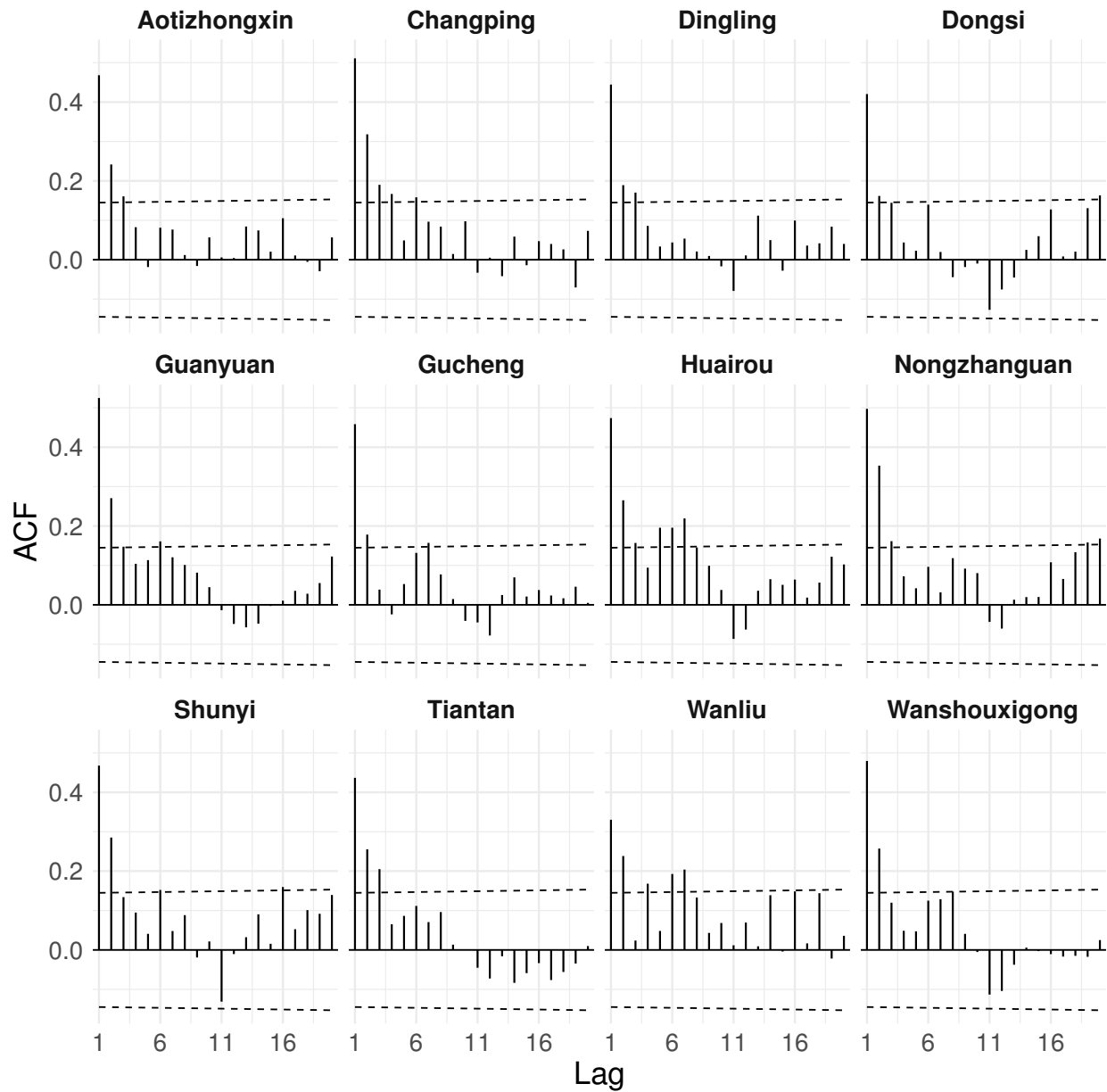


Figure 18: Beijing air pollutants data. Autocorrelation function of log-transformed CO concentrations, with missing values imputed using the station-wise mean.

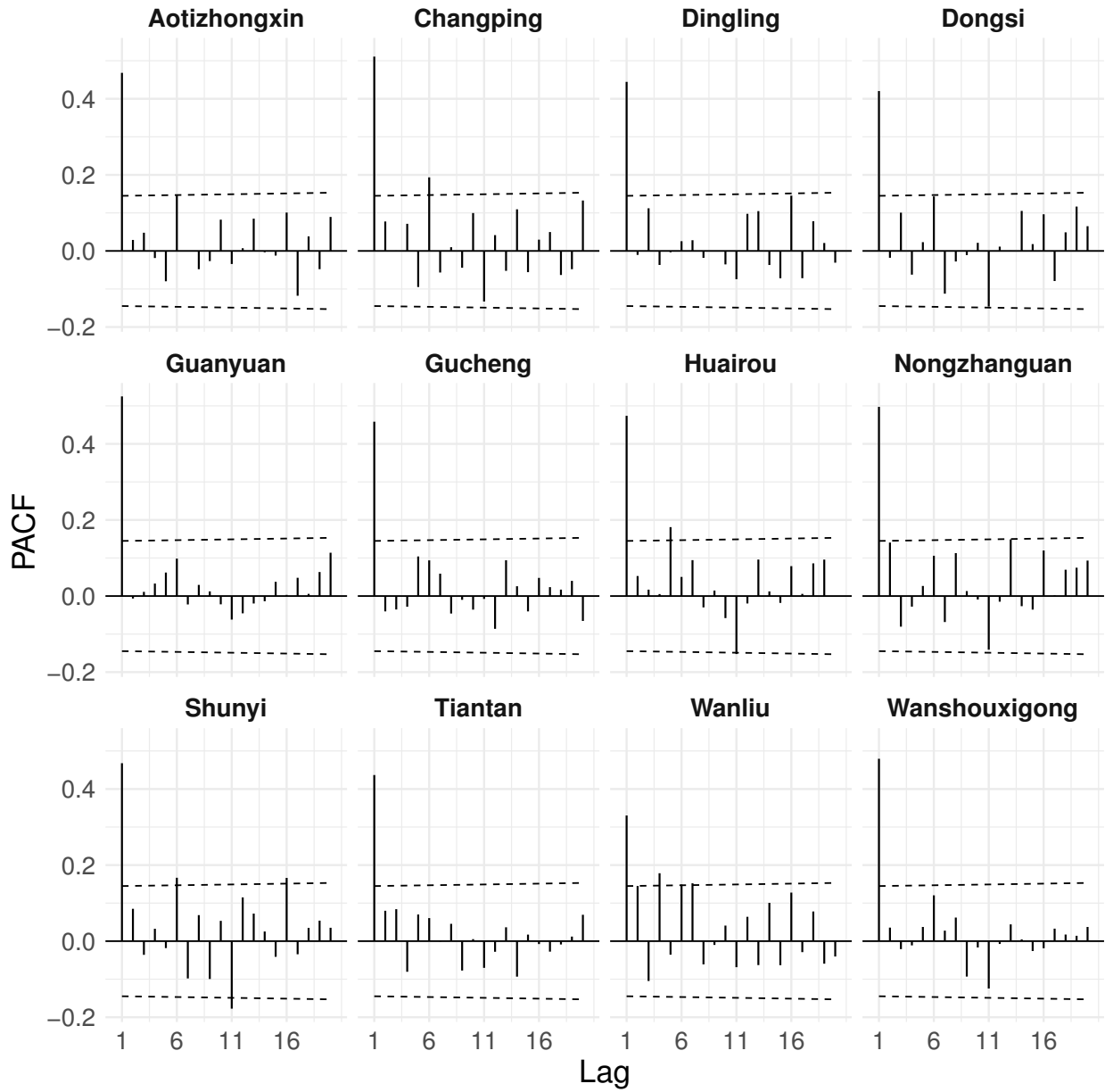


Figure 19: Beijing air pollutants data. Partial autocorrelation function of log-transformed CO concentrations, with missing values imputed using the station-wise mean.

Table 17: Beijing air pollutants data. Gelman and Rubin convergence test for the DAGAR model

	R (point estimate)	Upper CI
β_0	1.00	1.00
β_1	1.00	1.00
β_2	1.00	1.00
β_3	1.00	1.01
σ^2	0.99	1.00
ρ	1.00	1.01
γ	0.99	1.00
τ^2	1.00	1.00

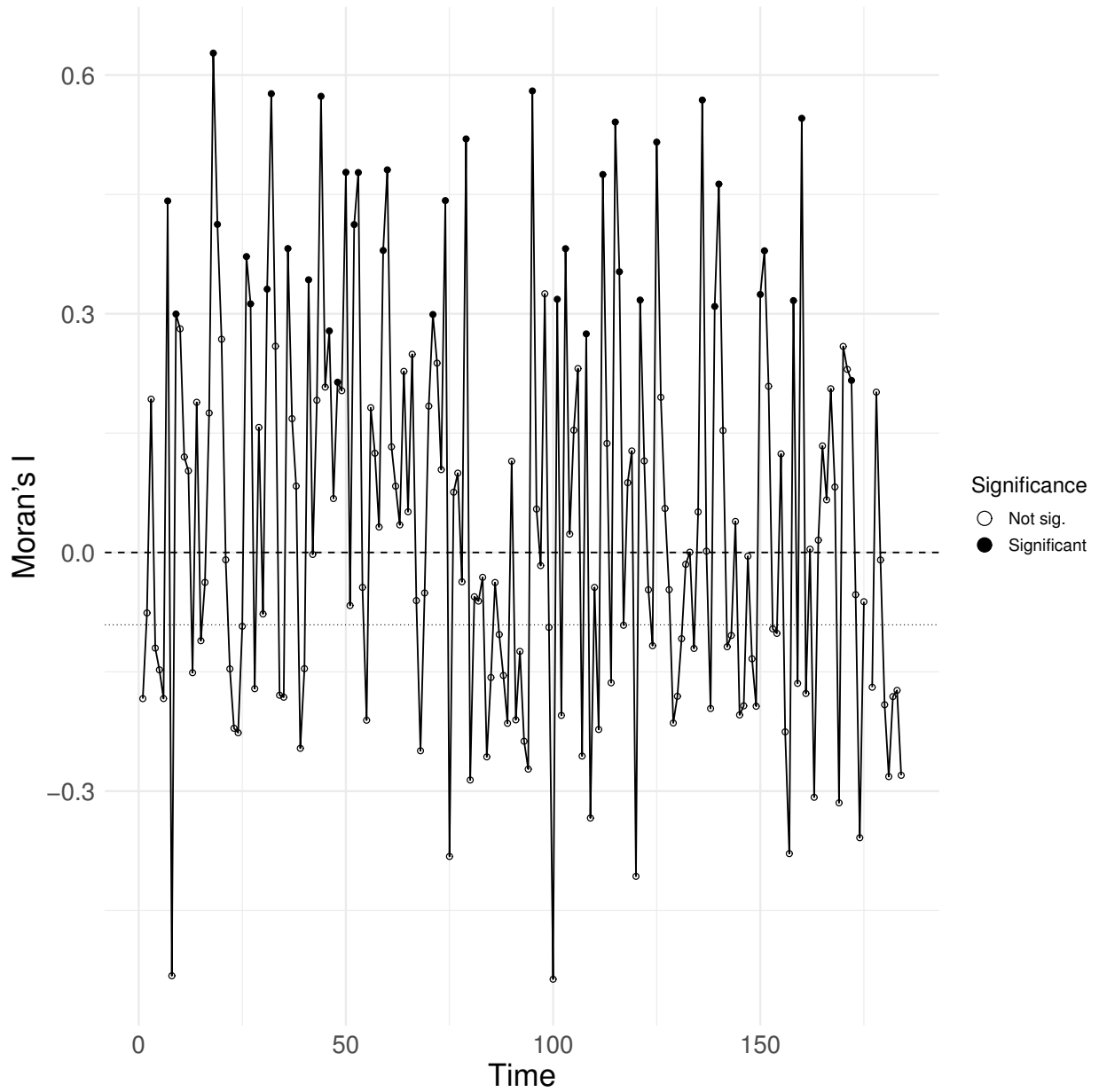


Figure 20: Beijing air pollutants data. Moran's I statistics for log-transformed CO concentrations at different time points, with missing values imputed using the station-wise mean.

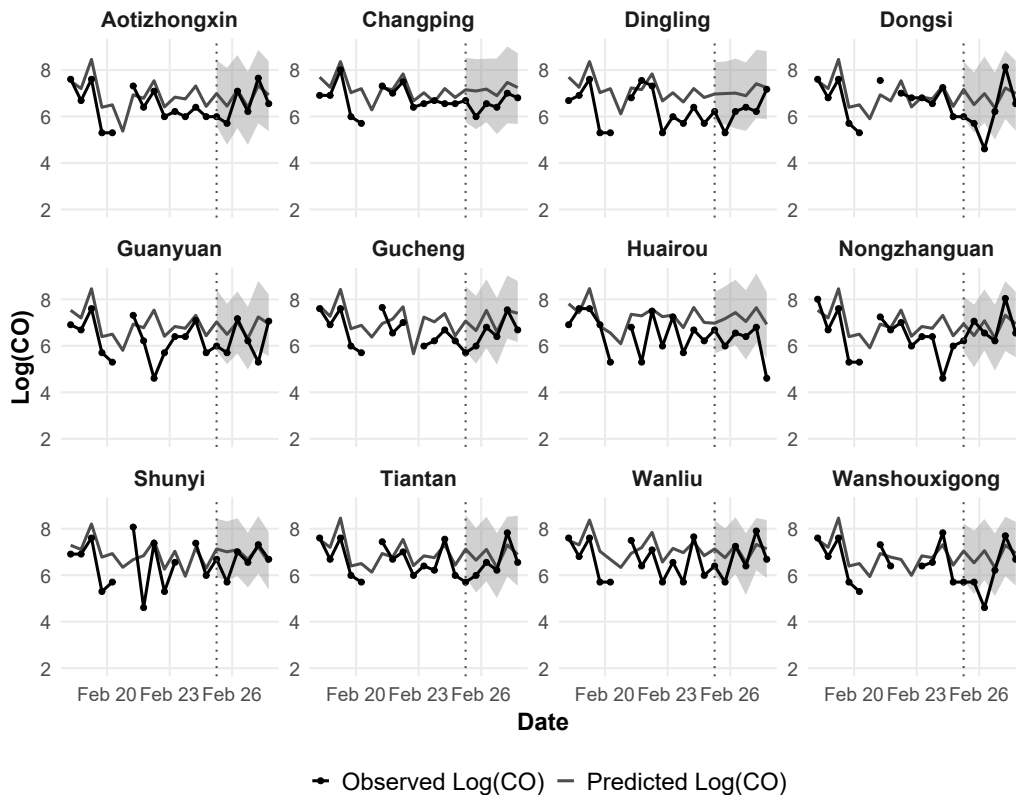


Figure 21: Beijing air pollutants data. Observed and predicted $\text{Log}(\text{CO})$ concentrations for the DAGAR model across 12 monitoring stations. The shaded areas represent 95% predictive intervals.

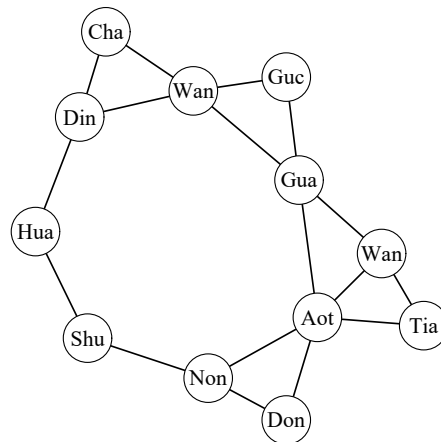


Figure 22: Beijing air pollutants data. Spatial network of the twelve air-quality monitoring sites in Beijing. The nodes correspond to monitoring stations used in the pollutant analysis, and the edges represent spatial neighborhood relationships.

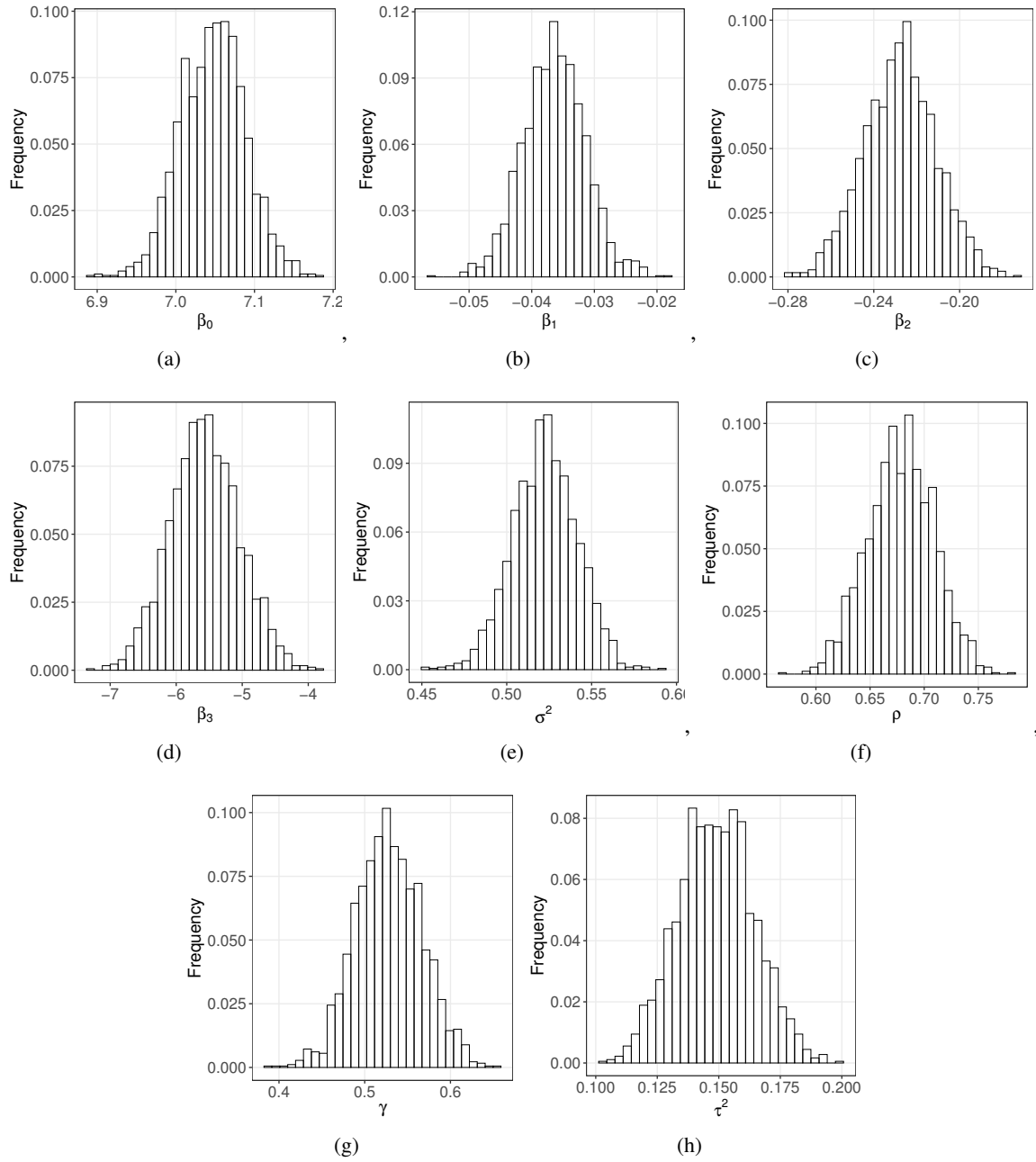


Figure 23: Beijing air pollutants data.. Posterior distribution of the parameters for the DAGAR -AR(1) model.

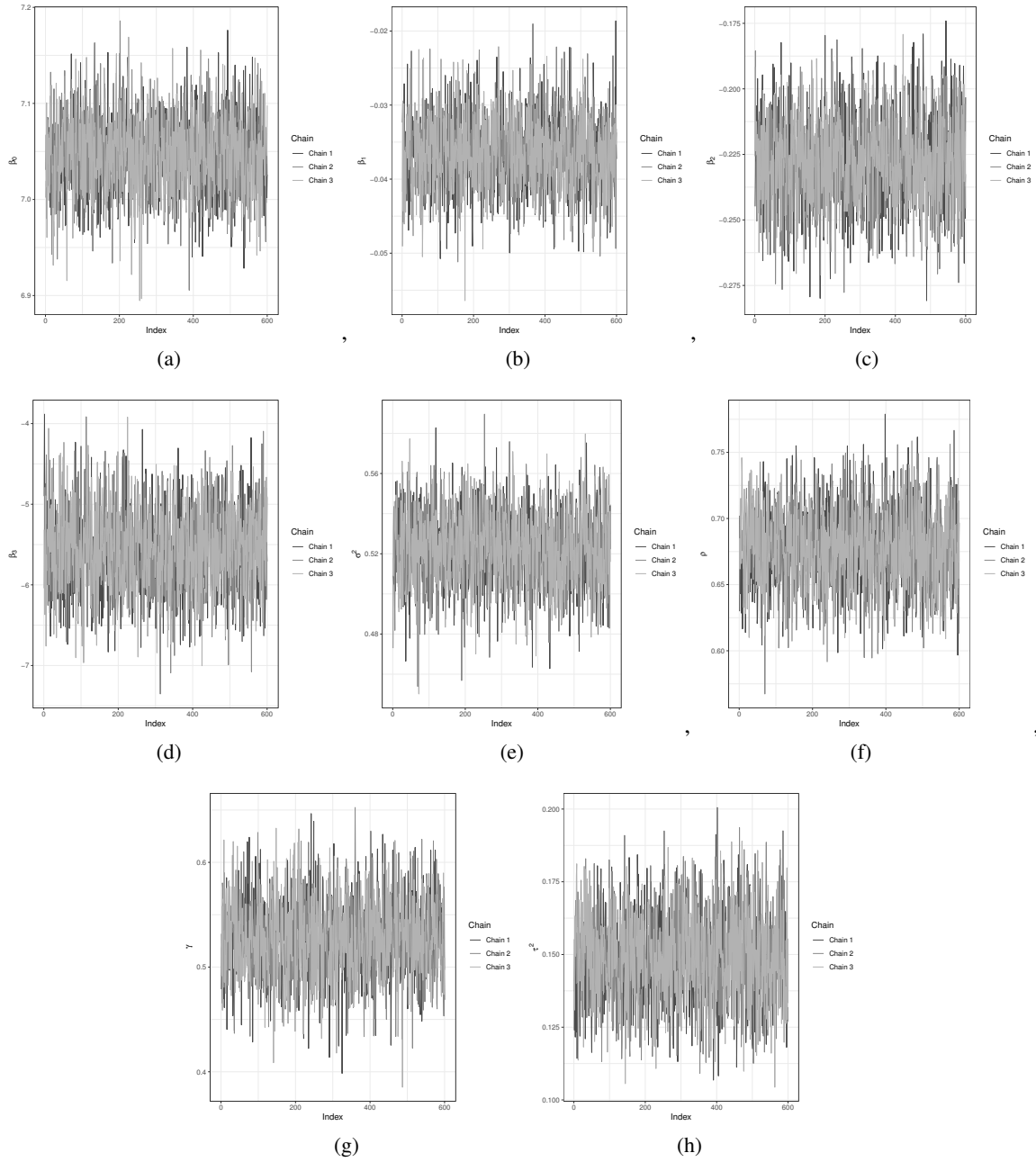


Figure 24: Beijing air pollutants data. Posterior chains of parameters for the DAGAR -AR(1) model.

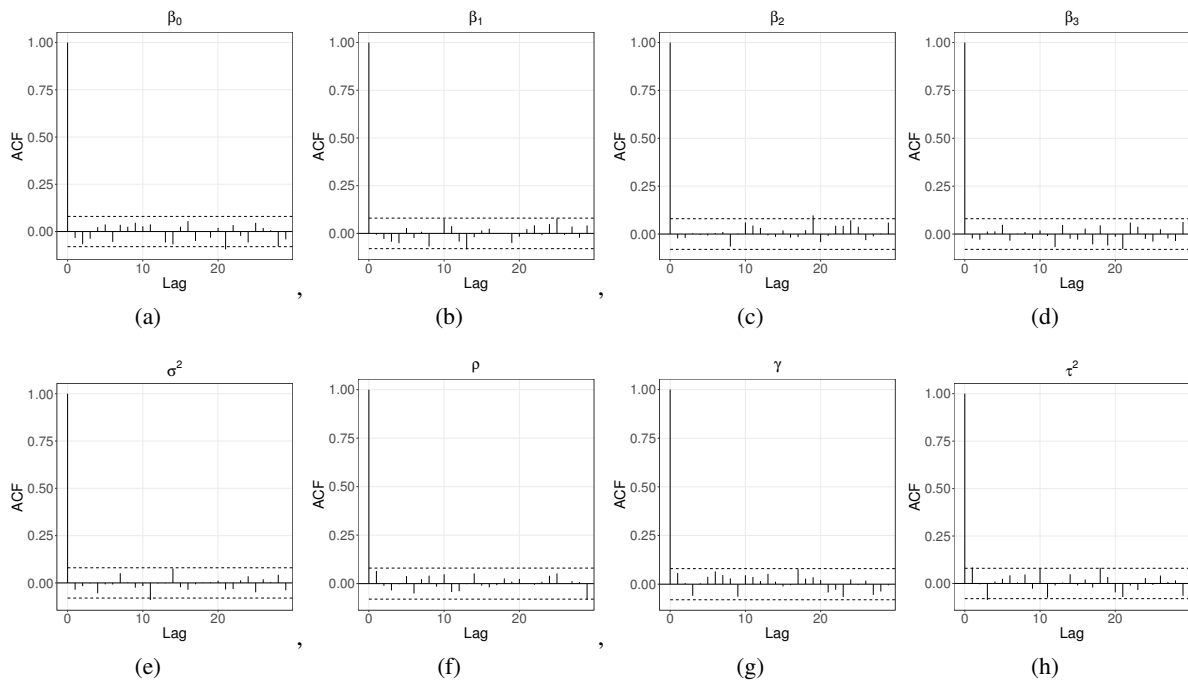


Figure 25: Beijing air pollutants data. ACF of the parameters for the DAGAR -AR(1) model.